Journal of Volcanology and Geothermal Research 464 (2025) 108349

Contents lists available at ScienceDirect

Journal of Volcanology and Geothermal Research

journal homepage: www.journals.elsevier.com/journal-of-volcanology-and-geothermal-research

Effects of lateral dyke propagation and pre-existing fractures on shallow deformation: Data from the Etna 1947 eruption and analogue models

A. Tibaldi [a,b], A. Luppino [a,*], E. De Beni [c], N. Corti [a,b], M. Cantarero [c], F. Pasquarè Mariotto [d], F.L. Bonali [a,b]

[a] Department of Earth and Environmental Sciences, University of Milan Bicocca, Milan, Italy
[b] CRUST – Interuniversity Centre for 3D Seismotectonics with Territorial Applications, Chieti, Italy
[c] National Institute of Geophysics and Volcanology, Etneo Observatory Section of Catania, Italy
[d] Department of Human and Innovation Sciences, Insubria University, Como, Italy

ARTICLE INFO

Keywords:
Dyke propagation
Pre-existing fractures
Mt. Etna
Surface deformation

ABSTRACT

Mount Etna, one of Europe's most active volcanoes, has experienced a variety of eruption settings throughout its history, including summit, lateral, and eccentric eruptions. In this study, we provide a detailed analysis of the structures formed during the 1947 lateral eruption, along the NE Rift, using historical aerial photos and accounts, archival images, and contemporary field and drone data. Photogrammetric processing of 1932 and 1954 aerial photos enabled us to map the structures formed before and during the eruption, in order to examine the effects of pre-existing fractures on the 1947 deformation pattern. With the aid of field surveys, we studied 90 normal faults, 194 dry fractures and 17 eruptive fissures, collecting data on the structures' length, azimuth, vertical offset, vectors and amount of opening. The reconstruction of a detailed chronology of the eruption's day-by-day development, allowed us to characterize the event as a NE-directed, lateral propagation of magma along a N-S to NE-SW-striking dyke, which followed the path of a previous similar event. Based on the reconstruction of the fault-slip profiles at both sides of various 1947 grabens, we were able to show that fault scarps taper towards NE. Analogue models were also used to simulate the lateral intrusions of dykes and the consequent formation of shallow structures. All the data suggest that the formation of the various structures, with different geometry and deformation, depends upon a combination of magma overpressure, local topography, external stresses, pre-existing structures, and direction of magma propagation.

1. Introduction

At volcanoes, magma can either rise along the main central conduit, triggering summit eruptions, or through their flanks, producing lateral eruptions. Magma moving underneath the flanks can reach the surface at lower altitudes, where it can feed lava flows that can travel as far as urbanized areas, and sometimes directly affect villages. Moreover, shallow magma movements trigger important deformation of the topographic surface, possibly producing bulging of the ground, as well as faults and fissures (Rubin and Pollard, 1988; Gudmundsson, 2011a). Understanding the factors that control magma ascent and associated deformation at volcanoes is key to contributing to the evaluation of hazards due to volcanic unrest.

Magma transport in volcanoes and in the shallow crust occurs in the form of tabular bodies, i.e. dykes, inclined sheets and sills (Bates and Jackson, 1987; Ferrari et al., 1991; Acocella and Neri, 2009; Acocella et al., 2009; Tibaldi et al., 2011; Magee et al., 2012; Geshi and Neri, 2014; Falsaperla and Neri, 2015; Tibaldi, 2015; Bonali et al., 2015; Acocella, 2021). Below volcano flanks, magma most commonly moves along vertical to subvertical dykes. Magma overpressure ruptures the host rock ahead of the dyke tip to form tensile fractures that open perpendicular to their planes (Mode I fractures, Anderson, 1951; Rubin and Pollard, 1987; Rubin, 1993), a process that in turn allows further magma propagation (Gudmundsson, 2011b). These dykes may undergo vertical (Sato and Hamaguchi, 2006) or lateral (Wright et al., 2006; Paquet et al., 2007) dominant propagation. Several factors have been proposed to predict whether a dyke will propagate laterally or vertically, including buoyancy (Takada, 1990; Lister and Kerr, 1991; Menand and Tait, 2002; Townsend et al., 2017), different mechanical properties of layers providing barriers to magma ascent (Rivalta et al., 2005;

* Corresponding author.
E-mail address: a.luppino6@campus.unimib.it (A. Luppino).

https://doi.org/10.1016/j.jvolgeores.2025.108349
Received 11 February 2025; Received in revised form 24 April 2025; Accepted 28 April 2025
Available online 30 April 2025

Gudmundsson, 2006; Kavanagh et al., 2006; Maccaferri et al., 2011), closure or opening of the central conduit (Acocella and Neri, 2003; Lanzafame et al., 2003; Acocella et al., 2006), topographic reliefs inducing lateral stress gradients (Fiske and Jackson, 1972; Fialko and Rubin, 1999; Muller et al., 2001; Acocella and Neri, 2009; Kervyn et al., 2009; Maccaferri et al., 2016; Pinel et al., 2017), or rotation of the principal stress axes (Dahm, 2000; Watanabe et al., 2002; Bagnardi et al., 2013; Corbi et al., 2015, 2016). In particular, the load of large volcanic edifices favors lateral dyke propagation (Pinel and Jaupart, 2004), as attested by the higher frequency of laterally propagating dykes in central volcanoes (Acocella and Neri, 2009).

In spite of the numerous works focused on the factors that condition lateral vs vertical dyke propagation, fewer studies have been conducted on the deformation pattern that can result from one type of propagation compared to the other. Most research, in fact, is dedicated to gain insight into the factors that can generally contribute to dictating the dyke-induced surface deformation, such as different geometries of the intrusion plane, the dissimilar mechanical layering of the host rock, and topographic effects (Acocella et al., 2006, 2009; Neri et al., 2008; Bonforte et al., 2009; Battaglia et al., 2011; Trippanera et al., 2014, 2015; Galland et al., 2015; Guldstrand et al., 2017; Fittipaldi et al., 2019; Gudmundsson, 2020; Tibaldi et al., 2022). Instead, detailed studies on surface deformation induced by laterally-propagated dykes are scarce (e.g. Hjartardóttir et al., 2016; Ágústsdóttir et al., 2016), mainly due to the difficulty of establishing with sufficient reliability the dyke flow direction associated with surface fracturing. More work is also needed to analyze in the field how pre-existing fractures interact with the development of further deformation triggered by a successive propagating dyke (e.g. Ruch et al., 2016; Hjartardóttir et al., 2023; Døssing et al., 2024). To accomplish this, a detailed structural map is needed, showing the fracture field before a new dyking event.

Through this work, we aim to evaluate the deformation pattern associated with a lateral dyke propagation, keeping into account the role of pre-existing fractures, based on an in-depth analysis of the 1947 CE Mt. Etna eruption, Italy (Fig. 1). This eruption occurred along the northern volcano flank in February–March 1947, following several events that took place at the summit craters, including a subplinian eruption (Silvestri, 1949; Branca and Del Carlo, 2005). The analysis of chronicles in local newspapers and published papers enabled us to suggest that the 1947 event was produced by the lateral propagation of a dyke. By analysing aerial photos of pre- and post-1947 surveys, we were able to reconstruct, at a very high detail, the fracture field present in the area before the eruption, as well as the fissures and faults produced by the 1947 event. 3D topographic models produced from the aerial historical photos enabled us to reconstruct fault slip profiles, integrated by new structural field mapping and Unmanned Aerial Vehicles (UAV) surveys, aimed at assessing deformation and kinematic parameters along the fractures. The above volcanotectonic data were enriched by analogue modelling of surface deformation induced by lateral dyke propagation.

A better understanding of these events not only deepens the knowledge of the geological-structural history of Mt. Etna, but represents a useful example for improving the general understanding of magmatic intrusion-related deformation. Ground truth data like those presented here may also constitute the basis for further analogue or numerical modelling of lateral dyke propagation processes. Therefore, the main scientific questions addressed in the present work include: i) what was the main magma flow direction during the 1947 event? ii) Does a lateral dyke propagation produce a special pattern of faults? iii) How do pre-existing fractures influence successive dyke-induced deformation events?

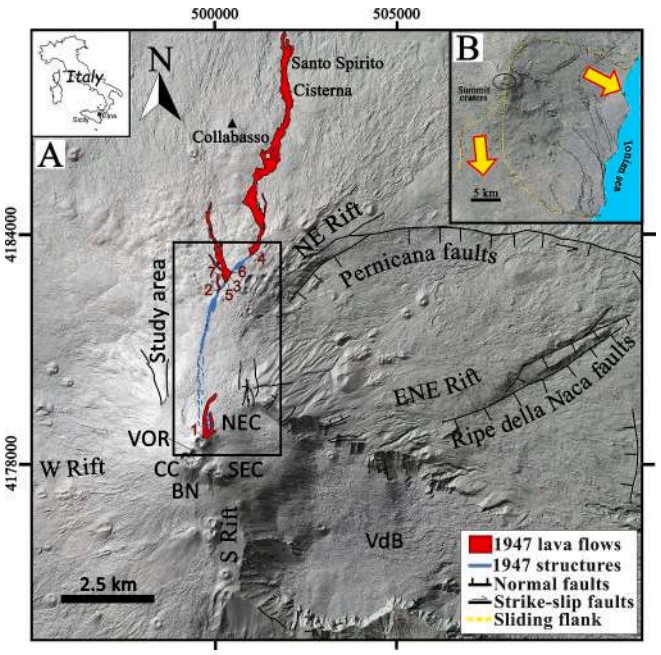

Fig. 1. (A) Shaded view of the central-northern sector of Mt. Etna, with the 1947 lava flows and the structures that formed during the 1947 event (blue lines). Main faults are indicated with black lines (from Azzaro et al., 2012). Ticks indicate the downthrown sector of normal and transtensional faults. Numbers in red give location of the 1947 vents that opened in sequence from 1 to 7. CC = Central Crater, NEC = North East Crater, SEC = South East Crater, VOR = Voragine crater, BN = Bocca Nuova crater, VdB = Valle del Bove. (B) Shaded view of the central-eastern part of the volcano with areas affected by sliding (yellow arrows indicate the main directions). Boundaries of sliding sectors (yellow lines) from Borgia et al. (1992), Rust and Neri (1996) and Tibaldi and Groppelli (2002). The resolution of this model is 2 m/pixel. Reference system: UTM33-WGS84. (For interpretation of the references to colour in this figure legend, the reader is referred to the web version of this article.)

2. Geological background

2.1. General framework

Mt. Etna, the largest active volcano in continental Europe, initiated its growth through submarine eruptions around 500 ka BP. The subsequent northwestward migration of subaerial volcanism led to the development of a small shield volcano (220–120 ka BP), followed by the emergence of multiple polygenetic centers (110–60 ka BP) now underlying the Valle del Bove (VdB; Fig. 1, Branca et al., 2008, 2011a, 2011b; De Beni et al., 2011). A later eruptive phase gave rise to two stratovolcanoes: the Ellittico (57–15 ka BP) and the Mongibello (15 ka BP–present), which dominate the central Etnean edifice. Around 10 ka BP, a sequence of slope failures generated the amphitheater-shaped depression of the VdB (Fig. 1; Guest et al., 1984a; Calvari et al., 1998a, 2004; Malaguti et al., 2023), which today channels most of the lava flows originating from the summit craters (Branca et al., 2011a).

In the last millennia, Mt. Etna's activity has been documented since the Greek and the Roman civilizations, giving volcanologists a uniquely long historical record for an active volcano (Branca and Del Carlo, 2004). Concerning the summit part of Mt. Etna, according to historical memories, the Central Crater (CC) was the undisputed ruler of the volcano at least until 1911 CE, when the formation of a pit crater located north-east of the CC and followed by a series of subterminal eruptions gave rise to the North East Crater (NEC). From 1911 to the second half of the 20th century, nearly all the lateral eruptions originated in the north-eastern and eastern sectors of Mt. Etna, while only the 1942 CE eruption occurred in the southern part of the volcano. Also the CC underwent

some changes: in 1945, a new pit crater named Voragine (VOR) was formed, and in 1968 the Bocca Nuova (BN) crater flanked them. In 1971, the South East Crater (SEC) was generated, and since then most of the lateral eruptions have occurred in the southern flank of the volcano, proving that the lateral eruptive activity is strictly correlated to the summit activity (Branca and Del Carlo, 2004, 2005; Branca et al., 2011a, 2011b; Proietti et al., 2023).

The lateral eruptive activity of the volcano has been mainly concentrated along four weakness zones, namely West, South, East-North-East, and North-East Rift (W, S, ENE and NE Rift, Fig. 1) (Lo Giudice et al., 1982; Tibaldi and Groppelli, 2002; Azzaro et al., 2012; Cappello et al., 2012). The area of the present study belongs to the NE Rift, which is constituted of swarms of dry fissures, eruptive fissures, and faults, punctuated by several pyroclastic cones aligned and elongated from NNE to NE (Lo Giudice et al., 1982; Azzaro et al., 2012). The rift extends for 7 km, with an average width of 500 m, from over 2500 to 1700 m a.s.l. (Tibaldi and Groppelli, 2002). The southern flank of the NE Rift gradually transforms into the Pernicana Fault (Fig. 1, Groppelli and Tibaldi, 1999; Branca et al., 2011a; Barreca et al., 2013), a left lateral-normal fault that confines to the north the instability of the volcano's eastern flank (Cannata et al., 2021).

Among all the eruptions that affected the NE rift, some of them deserve to be mentioned since their products have or could have had consequences on the eruption that we are examining in this work. The 1614–24 CE eruption is one of the longest-lasting in the recorded history of Mt. Etna (Branca et al., 2011a); its products covered an area of over 21 km^2 corresponding to a total volume of 1–2 km^3 of lava (Guest et al., 1984b). In the following century, only the 1764–65 CE event produced important products on the NE flank of Mt. Etna. The information about this eruption is very fragmented, but according to historical maps (e.g. Waltershausen, 1880) the lava field covered an area longer than 4.5 km reaching a minimum elevation of 1660 m a.s.l. (Branca and Del Carlo, 2004). The 1809 CE event also affected the study area, and was marked by two eruptive fissures: a main one extending for 4250 m from the summit CC to 1300 m a.s.l., and a 1200 m-long one located nearly half a kilometer to the north (Geshi and Neri, 2014). Finally, another important event is the 1874 CE eruption, which consisted in a 4000 m-long fracture system that produced a 800 m-long lava flow at 2160 m a.s.l. (Silvestri, 1874). Now, this lava flow is partially covered by the 1947 CE deposits.

2.2. The 1947 eruption chronology

From January 1947, the summit craters (NEC and CC) were in volcanic unrest after two years without intense activity. This unrest, whose peaks were originally described as lava fountains by Silvestri (1949) and later as sub-plinian eruptions (Branca and Del Carlo, 2005), occurred first in the NEC on the 5th and 6th of February 1947. A few days later, on February 10th, the NEC produced a paroxysmal episode with 600-m-high lava fountains and later, on the 16th of the same month, the CC did the same. In addition, the collapse of the VOR that occurred in January increased considerably the diameter of this crater, from about 5 m up to more than 200 m (Silvestri, 1949). According to Silvestri (1949), these episodes could have obstructed the central conduct, hindering magma rising and leading new magma to propagate laterally towards the NEC.

On February 24th, a fissure opened at the base of the NEC, and in a few hours (La Sicilia, 26 February 1947; Ponte, 1947a, 1947b, 1948; Silvestri, 1949) it propagated 6 km towards NE following the NE Rift (details in Table 1). On the same day at 10:00 pm, a first eruptive fissure opened at 3050 m a.s.l., producing Vent 1 (Fig. 1). Based on Ponte (1947a), a few hours later, a series of eruptive vents opened at 2350, 2300 and 2070 m.a.s.l. (Vents 2, 3 and 4), giving birth to six different lava flows.

In the following days and until February 26th, only the downstream fissure was continuously fed, producing a lava flow over four days that extended 8 km reaching a minimum altitude of 880 m a.s.l. The localities of Collabasso, Cisterna and Santospirito (Fig. 1) were affected by the lava flow and part of the Castiglione woods were destroyed, along with numerous vineyards. The nearby town of Passopisciaro was temporarily evacuated due to the threat posed by the lava, which fortunately came to a stop, leading to the destruction of only a few houses (La Sicilia, 27 February 1947). On February 26th, a new vent also opened at 2300 m a.s.l. (Vent 5).

On the night of February 27th, the lava flows fed by Vent 4 stopped, while a new vent opened at about 2300 m a.s.l. (Vent 6). On March 5th, a vent opened again at 2300 m a.s.l., feeding another lava flow (Vent 7). On the same day, between Vent 4 and 6, an "intumescence" (Silvestri, 1949) started to form, which is to say an uplift.

The eruption finally halted on March 8th, with the most advanced lava front that stopped only a few kilometers from the cities of Randazzo and Linguaglossa (La Sicilia, 9 March 1947).

Table 1
Evolution of the eruptive fissures that generated lava flows and eruptive vents.*

Sequence	Day and time	Elevation	Fissure length	Reference
1	Feb 24, h 10 p.m.a,b	3050 m a.s.l.	128 m	Silvestri, 1949 Ponte, 1947a, b
2	Feb 24, 10 p.m.a, few hours after 10 p.m.b	2350 m a.s.l.	177 m	Silvestri, 1949 Ponte, 1947a, b
3	Feb 24, h 10 p.m.a, few hours after 10 p.m.b	2300 m a.s.l.	36 m*	Silvestri, 1949 Ponte, 1947a, b Photo by Reiner
4	Feb 24, h 10 p.m.a, few hours after 10 p.m.b	2070 m a.s.l.	356 m	Silvestri, 1949 Ponte, 1947a, b La Sicilia 26/2/1947
5	Feb 26, night	2300 m a.s.l.	138 m*	Silvestri, 1949 Ponte, 1947a Photo by Taffara
6	Feb 27, night	2300 m a.s.l.	320–325 m*	Silvestri, 1949
7	Mar 5, h 11 a.m.	2300 m a.s.l.	325 m	La Sicilia 6/3/1947 Silvestri, 1949
Undefined	Undefined	2540 m a.s.l.	57 m	Silvestri, 1949 Our data

* From historical photos.

3. Methodology

The study of the volcanotectonic evolution of the 1947 eruption was performed through a multidisciplinary approach based on: *i)* historical data aimed at establishing the timing of the various events and dyke propagation; *ii)* analysis of historical aerial photos to map the 1947 fracture field, as well as the pre-existing structures; *iii)* field and UAV surveys to collect further quantitative data; *iv)* analogue modelling to better understand the evolution of the fracturing process. In the following sections, we provide details for each of them.

3.1. Historical chronicles

We collected all the available historical information regarding the timing of the various events that accompanied the 1947 eruption, including explosions from pre-existing and new craters/vents, lava flows and fracture field growth. This step was fundamental since part of the structures related to the 1947 eruption is nowadays covered by new lava flows and pyroclastic deposits (Romano and Sturiale, 1982; Branca et al., 2011a). The main sources are: i) several ground photos found in state archives and library, in particular photos taken by plane by Captain G. Reiner and M. Taffara in the year 1947 and photo included in Ponte

(1947a), Silvestri (1949) and Bonaccorso and Branca (2010); ii) a written report and a 1:20,000 map from Silvestri (1949); iii) daily news from "LA SICILIA" (La Sicilia, 1947), a local newspaper that provided a detailed sequence of the time of opening of some eruptive fissures and vents, and lava flows.

3.2. Mapping from historical aerial photos

The overall mapping of the surface structures related to the 1947 eruption, including eruptive fractures, dry fissures and lava flows, was performed on two photogrammetry-derived orthomosaics (OMs, Figs. 2A and B). We used 149 historical stereoscopic aerial photos, dating to the closest time frame prior and after the event (1932 and 1954), in much the same way as Bonali et al. (2024a), who performed a similar analysis on the 1971 Mt. Etna event. These OMs were obtained by processing two sets of photos from the Istituto Geografico Militare (IGM, https://igmi.org/) through the software Agisoft Metashape®.

We used a total of 22 Ground Control Points (GCPs) to georeference and scale the 1954 OM using 2022 Google Earth Pro satellite imagery. 14 of these GCPs were subsequently employed to georeference and scale the 1932 OM over to the 1954 ones. GCPs were selected based on stable long-term surface features such as artefacts, pyroclastic cones and lava flow boundaries, which have remained unchanged over the past century. The resulting resolution of the two OMs was 29 cm/pixel (more details about the methodology in Bonali et al., 2024a). The two OMs covered the northern part of the 1947 fracture swarm (Figs. 2A and B) where we distinguished: i) the structures that are present only in the 1932 OM (classified as pre-existing, Fig. 2E); ii) fractures that are present in the 1954 OM showing an increase in length with respect to 1932 (classified as reactivated, Figs. 2F); iii) fractures that are present only in the 1954 OM, and were absent in 1932 (classified as newly formed, Figs. 2C and D).

3.3. Field surveys and UAV quantitative data collection

Following the initial structural mapping on historical OMs, we performed a more quantitative analysis to distinguish between extension fractures (fissures, Fig. 3), faults and eruptive fissures (Fig. 4) as well as to recognize areas with uplifted or downthrown blocks, and the presence of grabens (Fig. 4A). Specifically, structures displaying vertical offset were classified as normal faults, while those characterized only by wall separation were classified as fissures (extension fractures). Additionally, in the presence of erupted materials, such as lava flows or scoria deposits, we further classified these structures as eruptive fissures, in contrast to dry fissures, where no volcanic activity was observed.

This approach was aimed at quantifying: *i)* the kinematics, vertical offsets and slip profiles along faults; *ii)* the amount and direction of the opening vector along fissures; iii) the amount of opening along the eruptive fissures.

These measurements were performed by classical field surveys, and by the analysis of high-resolution 3D models, Digital Surface Models (DSMs) (e.g. in Fig. 5) and OMs derived from photogrammetry processing applied to UAV-collected pictures. We also checked some data using Immersive Virtual Reality (e.g. Tibaldi et al., 2020a; Antoniou et al., 2020; Harknett et al., 2022; Bonali et al., 2024b). Quantitative data derived from these models are considered as reliable as field-collected ones, as highlighted in the literature (Bonali et al., 2019; Tibaldi et al., 2020a). UAV surveys were performed by way of a DJI Mavic 3 T (1/2-in. CMOS, effective pixels: 48 MP) equipped with an RTK module that guarantees centimeter-level accuracy when used with the Network RTK service. The GNSS RTK receiver was connected to the SICILI@NET permanent reference station network of the INGV-OE (https://www.ct.ingv.it/index.php/risorse-e-servizi/sicil-net). During the UAV surveys, over 1000 photos were collected at an altitude ranging between 80 and 100 m above the takeoff point, allowing us to produce DSMs with a resolution of 3.4 cm/pixel and OMs with a resolution of 2.3 cm/pixel. The total covered area is 1.65 km^2.

Slip profiles, also termed displacement-length profiles, give a representation of the scarp height as a function of the distance measured along the fault. This is considered an indication of the possible direction of propagation of the fault plane (Manighetti et al., 2001; Tibaldi et al., 2020b; Pedicini et al., 2024). In the present work, slip profiles were

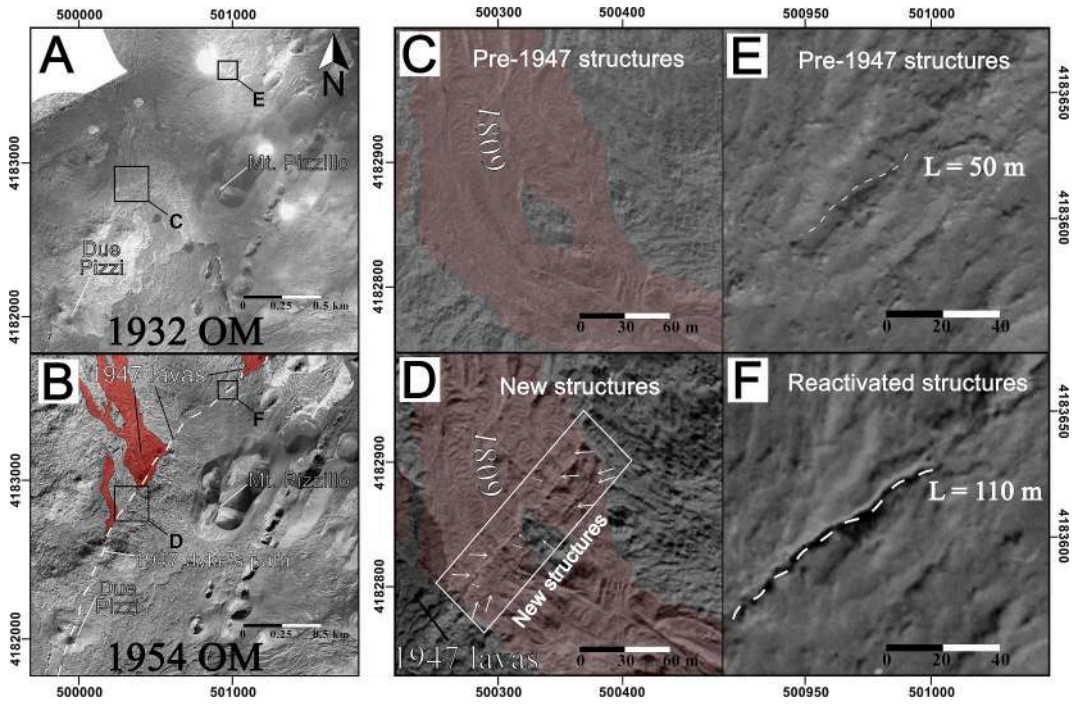

Fig. 2. (A) 1932, and (B) 1954 OMs. (C) and (E) are zooms of (A) showing: (C) an area with no pre-existing structures on the 1932 OM, and (E) an area with a single pre-existing structure (measured length = 50 m). (D) and (F) are zooms of (B), showing the same areas, but on the 1954 OM: in (D), new structures (white arrows) were formed, in (F) the already existing structure was reactivated, with an increase in length and width. Reference system: UTM33-WGS84.

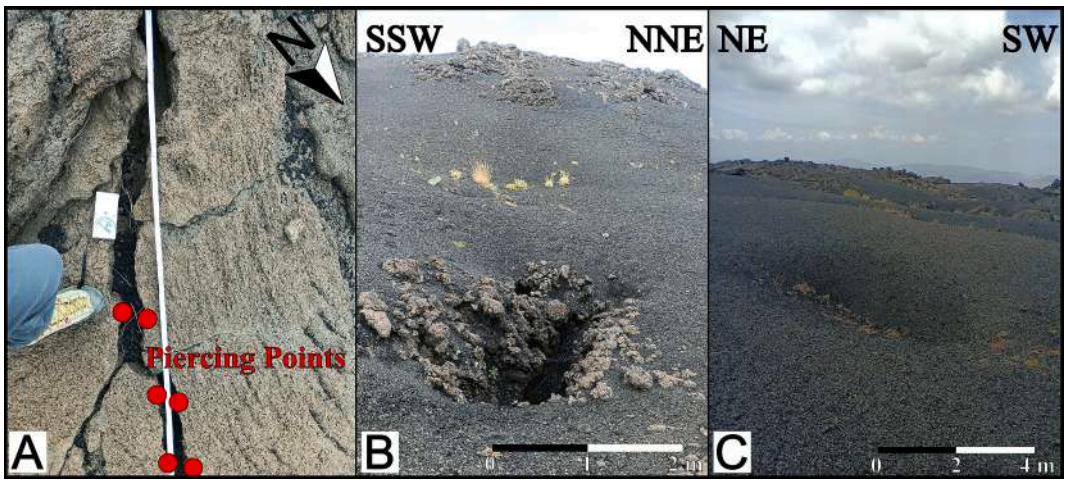

Fig. 3. Structures classified as fissures. (A) Exposed extension fracture; the white line represents the average fissure strike, red dots show piercing points, (B) partially covered extension fracture, and (C) hidden extension fracture inferred from sinkhole alignment and elongation. (For interpretation of the references to colour in this figure legend, the reader is referred to the web version of this article.)

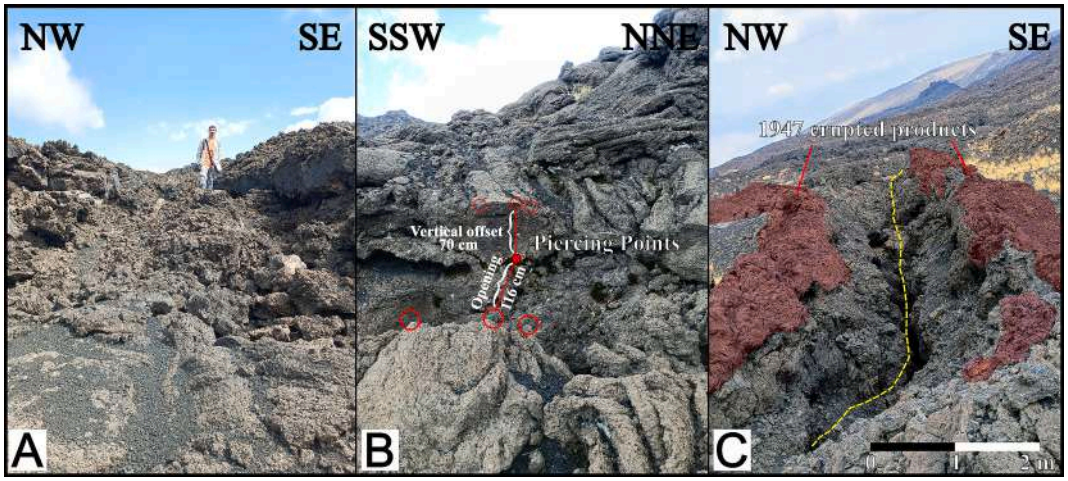

Fig. 4. (A) Overview of a graben formed by the 1947 dyke propagation. (B) Close-up of a fault plane affecting the lava surface. Piercing points indicate measurable displacements, with a dip-slip of 70 cm and an opening of 116 cm, consistent with extensional kinematics. (C) Eruptive fissure trace (yellow dashed line) of the 1947 Etna eruption with erupted material on both sides of the fissure (highlighted in red). (For interpretation of the references to colour in this figure legend, the reader is referred to the web version of this article.)

obtained by cumulating the vertical offset measured along all the various fault segments that compose the NW and SE boundaries of the graben structures developed during the 1947 event. Measurements were done each 3 to 4 m along the fault trace.

3.4. Analogue modelling

The set-up is made of a box filled with a mixture of granular material that mimics the brittle crust. Before filling the box, we inserted a deformable casing in a vertical position that represents the external boundary of the simulated dyke (Fig. 6). The casing is closed on three sides, whereas it is open on the external wall of the box where a fissure in the box wall allows the insertion of vertical slates of cardboard. The cardboards move horizontally and are inserted one at a time, with differential degrees of advancement, to simulate the gradual intrusion of a laterally-propagating dyke with decreasing thickness with distance from the magma source (Fig. 6B). The dimensions of the sand box are 21.2 × 30.2 × 7.5 cm (height). The cardboard upper tip line is 2.5 cm below the surface. Each cardboard is 0.5 mm thick. We inserted a maximum of 28 cardboards corresponding to a maximum total thickness of 1.4 cm, and a minimum thickness of 0.4 cm.

We took a large number of partially superimposed photos of the sand surface during six steps of the experiments, in order to record the increments of deformation. Photos were taken with a digital camera with a resolution of 20 Mpx. For each experiment, we took the same number of photos, with the camera systematically placed in the same nadir and oblique position, and at the same distance from the sandbox, to better survey the faults. The data were subsequently processed with the software Structure from Motion by Agisoft Metashape® in order to produce 3D models.

Before conducting the experiments, our analogue models were geometrically and dynamically scaled (e.g., Ramberg, 1971; Merle, 2015, and references therein). The material properties and applied forces were required to conform to geometric and dynamic similarity principles (King Hubbert, 1951), while maintaining a consistent length ratio (h*) defined as:

$h^* = h_{Model}/h_{Nature}$ (Merle, 2015).

For geometric scaling, we applied a scaling ratio:

$$l^* = l_{Model}/l_{Nature} = 2 \times 10^{-3}$$

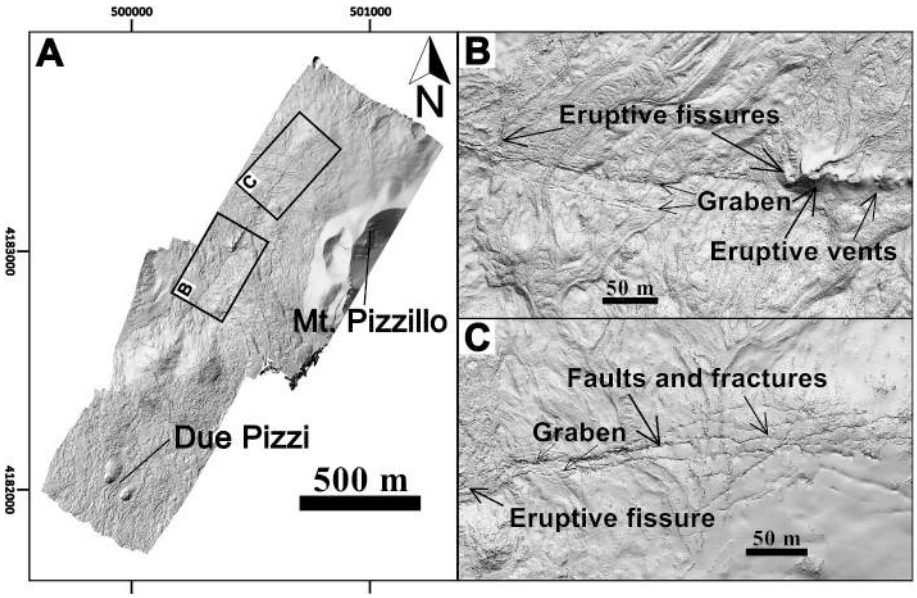

Fig. 5. (A) Shaded view of the DSMs obtained through UAV surveys and photogrammetry processing. The overall model was obtained by merging 4 different mosaics from 8 UAV surveys. In (B) and (C) details of selected areas, where two different grabens on the sides of an eruptive fissure are visible. The model resolution is 3.4 cm/pixel.

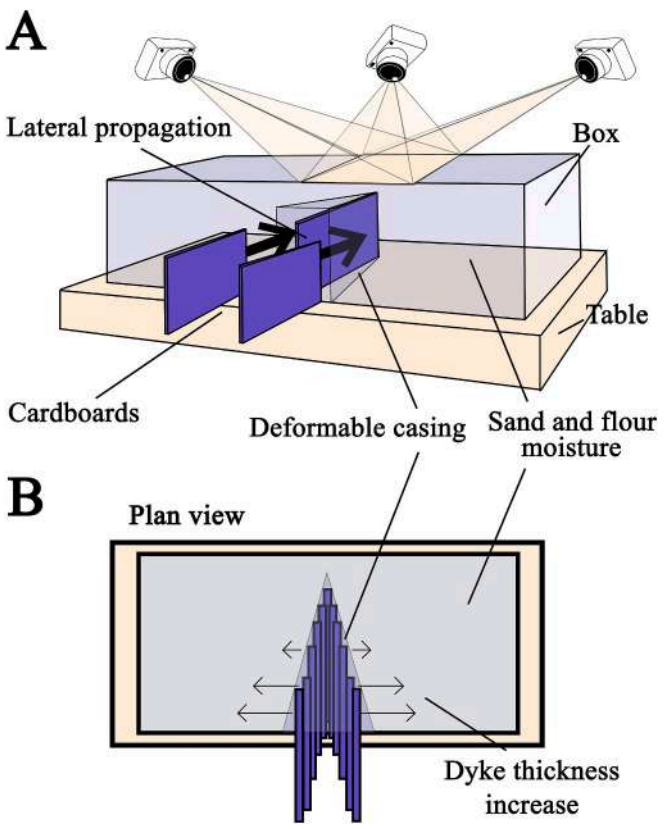

Fig. 6. Sketch of the analogue model setup. (A) 3D view of the sandbox, (B) plan view showing the arrangement of the vertical cardboard slates inserted one at a time to simulate the gradual intrusion of a dyke with decreasing thickness with distance from the source.

which means that 1 cm in the model corresponds to 5 m in the natural environment.

According to this scaling approach, the depth of the dyke tip in our models is at 2.5 cm, corresponding to a natural depth of approximately 13 m. This is a realistic estimate for the 1947 dyke based on the average width of the dyke-triggered grabens, as will be illustrated later in the text, and due to the fact that the dyke produced several vents along its path (this evidence attests its shallow depth). Additionally, the final dyke thickness in the model (ranging 4 to 15 mm), corresponds to 2–7.5 m; this is consistent with the thickness of the dyke from the 1809 Etna eruption (which also took place along the NE Rift), ranging from 2 m to several meters approaching the ground surface (Geshi and Neri, 2014).

The dynamic scaling factor, defined as the stress ratio $\sigma^* = \sigma$ Model/ σNature, is derived from the equation:

$\sigma^* = \rho^* \cdot g^* \cdot l^*$.

As the density of the analogue materials is approximately half that of natural rocks ($\rho^* = 0.5$) and that gravitational acceleration is identical in both the laboratory and nature ($g^* = 1$), the required stress ratio for a geometric scaling factor of 2×10^{-3} is: $\sigma^* = 1 \times 10^{-3}$. Considering that the cohesion of natural rocks typically ranges between 10^5 and 10^7 Pa (Hoshino et al., 1972; Glicken et al., 1980), the cohesion of the analogue material should be, in theory, between 100 and 10,000 Pa to maintain appropriate scaling. It is worth observing that in nature, values as high as 10^7 Pa are typically obtained from small laboratory samples (Schultz, 1996) or intact rock (Handin, 1966; Jaeger and Cook, 1969). Instead, field observations indicate that the lava flows forming the host rock are highly fractured due to cooling processes, as clearly shown also by the analyses reported in Bonali et al. (2024a) on the deposits characterizing Mt. Etna. Therefore, we believe that the adequate cohesion is in the range of 10^5–10^6 Pa for the in-situ rock. Consequently, the cohesion of the analogue material had to be within the range of 100–1000 Pa.

For our experimental tests, we used a mixture of sifted sand and wheat flour, representing two end-member analogue materials. This selection was intended to simulate brittle deformation in the upper crust (e.g., Walter and Troll, 2001; Holohan et al., 2005; Tibaldi et al., 2008a, 2008b; Acocella et al., 2013; Tortini et al., 2014; Bonali et al., 2018). The density of natural rocks typically ranges from 2000 to 3300 kg/m^3, with most common deposits in volcanic settings (intrusive rocks, basalts, etc) ranging between 2600 and 3000 kg/m^3 (Goodman, 1991). To simulate these conditions, we used a 50 %–50 % volume mixture of sifted sand and wheat flour with the following characteristics:

- Sifted sand: Bulk density of 1470 kg/m^3, grain size of 200–350 μm, and low cohesion of 30–40 Pa (Walter and Troll, 2001).

- Wheat flour: Bulk density of 700 kg/m^3 and cohesion of 330 Pa (Krantz, 1991).
- Final mixture: Bulk density of 1215 kg/m^3, measured internal friction angle (Φ) of 41°, and cohesion matching the scaling factor.

This composition ensures that the scaled density ratio and cohesion range resemble those of natural rocks.

4. Results

4.1. Eruption chronology vs fracture propagation

The analysis of all the available chronicles, integrated with new field data, allowed us to reconstruct the development of the 1947 events. The eruptive explosive episodes that occurred in the summit craters (CC, VOR and NEC) during the first month of 1947 were followed by the development of structures downhill of this summit zone, as shown in the sketch of Fig. 7. On the night of February 24th, a series of fissures started to propagate from the summit part of the volcano (3050 m a.s.l.) for over 6 km towards NE, with the lowest eruptive fissure at 2070 m a.s.l. In a few days, the eruptive fissures evolved, especially the one at 2300 m a.s.l., whose length passed from 36 m on February 24th to 138 m in two days, and then to 325 m in the last phase of the eruption (March 5th). Thus, in one day, the series 1 to 4 of vents gradually formed downhill (Fig. 7). From February 26th to March 5th, no more vents propagated downhill, and eruption activity focused at vents 5, 6 and 7.

Nowadays, the southernmost part of the strip affected by the 1947 structures is completely covered by lava flows and pyroclastic deposits from the 1949 eruption. The only available data on the 1947 structures here are from Silvestri (1949), who showed on a 1:20,000 map a 2.2-km-long area affected by 30 N-S-striking structures, without distinction between extension fractures or normal faults, with lengths from 31 to 212 m (southernmost box of Fig. 8A).

The dyke represented in Fig. 7 is an interpretation that will be described in the Discussion section.

4.2. Surveyed volcanotectonic structures

4.2.1. Geometry and distribution of structures

We collected new data by mapping all recognizable structures from the 1932 and 1954 aerial photographs along a total distance of 4 km, starting from the northern limit of the 1949 lava flows to the end of the 1947 structures northwards. We mapped these structures at a scale of 1:1000 on the OMs obtained by historical images. For the last 3 km, we mapped all the structures also in a scale of 1:100 based on the 2024 UAS-captured imagery and Digital Terrain Models (DTMs).

In Fig. 8A, it is possible to observe that the 1947 structures (in red) followed exactly a pre-existing swarm of fractures (in blue) for almost 6 km. Both swarms of structures start with a N-S strike in the southernmost part, then bend towards a NNE-SSW direction, and finally NE-SW in the northernmost part. A total of 112 pre-1947 structures were mapped, and their strikes were measured, showing a distribution that is consistent with the strike values of the 293 structures formed during the 1947 eruption (Fig. 8B). In Fig. 8C, we show the azimuth of fractures with respect to the distance from the initial, and southernmost, 1947 vent. The structures in the southernmost part of the area, mapped from Silvestri (1949), strike N170–190°E, with a dominant N-S orientation. Moving northwards, fracture strikes gradually bend from N-S, to NNE-SSW, and to NE-SW, designing an arc in plan view, with the concavity facing East. There are two zones, at 3.8 km and 4.9 km, which show a high dispersion of strike values. The zone at 3.8 km shows fracture strikes ranging in all directions; the zone at 4.9 km has fracture strikes ranging from NNW-SSE to E-W. It is worth noting that these zones of high dispersion of values coincide for the pre-1947 and the 1947

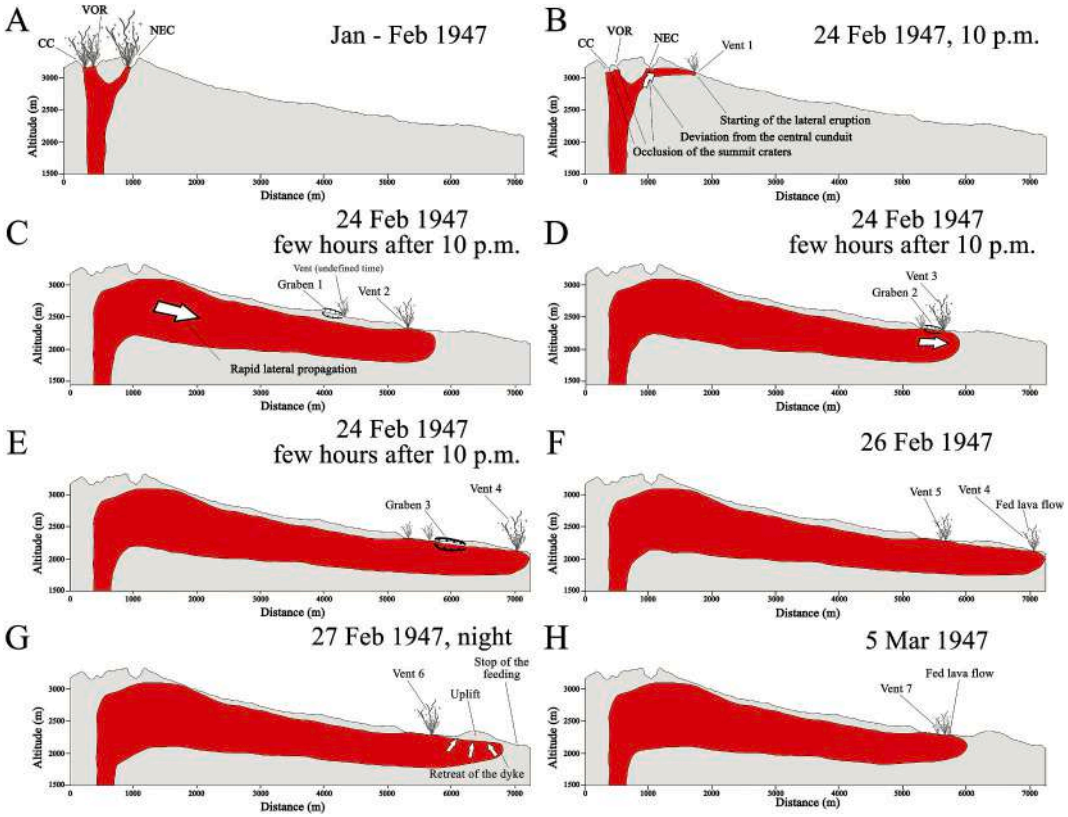

Fig. 7. Schematic section of the evolution of the 1947 Mt. Etna eruption based on the collected historical data and field checks. The sketch represents the shallower part of the volcano (above 1500 m a.s.l.). The height of the dyke is estimated based on data from the 2008 similar lateral intrusion (Currenti et al., 2011) and is just indicative. See text for details.

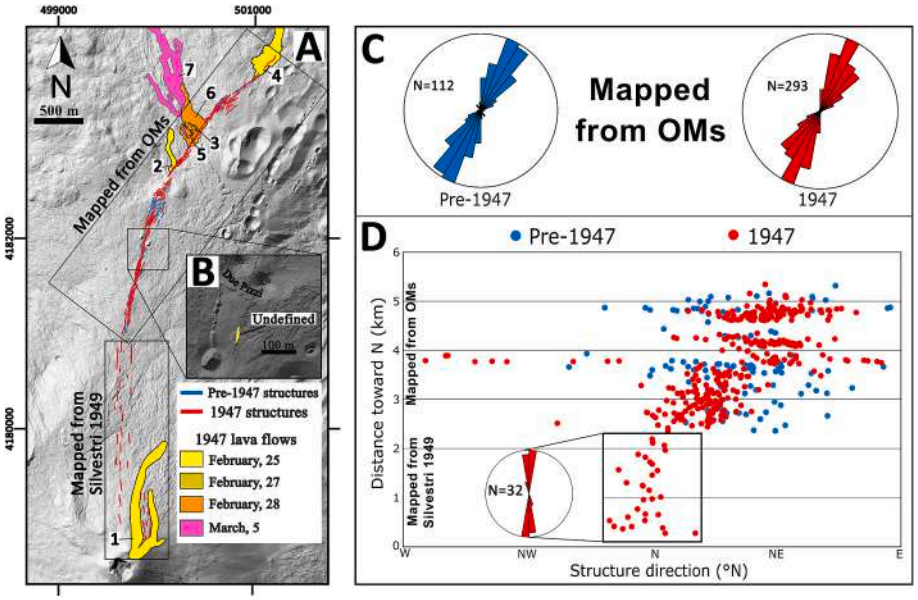

Fig. 8. (A) Shaded relief showing all the structures related to the 1947 event. The structures were arranged in two classes: i) fractures that are present only in the 1932 OM; ii) fractures that are present only in the 1954 OM (produced during the 1947 eruption). Numbers from 1 to 7 indicate the opening sequence of the eruptive fissures and the related lava flows (see Table 1 and Fig. 7 for more details). The small lava flow highlighted in yellow in the enlarged box (B) was produced during the 1947 events but the timing is not specified. (C) Rose diagrams of pre-existing and newly formed fractures mapped from the 1954 OM (upper box of Fig. 8A). (D) Graph showing azimuth of fractures with respect to the distance from the initial, and southernmost, 1947 vent. Structures in the southernmost part of the diagram are mapped from Silvestri (1949). Reference system: UTM33-WGS84. (For interpretation of the references to colour in this figure legend, the reader is referred to the web version of this article.)

structures.

A high-resolution geological map at a 1:1000 scale is presented in Fig. 9A, displaying all structures exclusively identified on the 1932 OM. As a consequence, this map represents the structural framework existing prior to the 1947 eruption.

These structures affect the lavas dated 1614–1624 CE, but stop in correspondence with the lava flow dated 1809 CE. This might constrain the event that created this swarm of fractures. In Fig. 9B, we report the structures mapped on the 1954 OM, from which we subtracted the structures already present in the 1932 OM. This figure depicts the new fractures developed during the 1947 event. In Fig. 9C, we report only the structures that were already present in the 1932 OM, but that result to be longer in the 1954 OM, thus representing the reactivated structures. It is straightforward to notice that the 1947 event reactivated 39 structures, corresponding to 35 % of the total pre-existing fractures in the area, with a significant increase in their length. Some of them (10 structures) were reactivated as eruptive fissures, generating eruptive vents and lava flows. The graph of Fig. 9D shows the length of pre-, *syn*-, and reactivated 1947 structures versus their strike. The longest fractures are those striking from N-S to NE-SW, consistent with the general orientation of the fracture swarms here. Regarding the three types of structures, there is no clear evidence of differences in length. The graph of Fig. 9E shows the strikes of the three types of structures versus northing. It can be noted that in the southern part of the area, there is an equal distribution of pre-, syn-, and reactivated 1947 structures. Towards the north instead, the reactivated structures are concentrated in three main areas that correspond to the zones of vent formation (Fig. 9C). It can also be noticed that both pre- and syn-1947 structures developed along the same strip of land. The graphs of Figs. 9 F, G and H show the distance towards the north of the structures versus their length for pre-1947, new syn-1947, and reactivated structures, respectively. In the first two types of structures, the fracture length decreases with northing, as quantified also by the regression line. Instead, for the reactivated structures, their length does not show a particular trend with northing.

4.2.2. *Differentiation in extension dry fractures, eruptive fissures and faults*

The classification of the structures in extension dry fractures, eruptive fissures and faults, is shown in Fig. 10. They were originally mapped at a scale of 1:1000, and classified using field data (1351 vertical offsets) collected in 2024, encompassing a total of 301 structures. Of the 301 structures, 90 are normal faults (53 NW-dipping and 37 SE-dipping), 194 are dry fractures and 17 are eruptive fissures. From this figure, it is possible to observe that SE- and NW-dipping normal faults are uniformly distributed in the central-northern sector of the studied area. In the southern part instead, dry fractures dominate (Figs. 10B and E). Fig. 10C and D show that SE- and NW-dipping normal faults mainly dip towards each other, creating narrow grabens. Finally, the rose diagrams of structure strike show a slight (10°) clockwise rotation of SE-dipping faults with respect to NW-dipping faults, and of eruptive fissures with respect to dry fractures (Fig. 10F).

The width of the fracture zone ranges from 120 m to a few meters, with the narrower zones in correspondence of the eruptive fissures. Two zones with the largest width are recognized, one to the south essentially made of dry fractures (Fig. 10B), and the other one to the north made of both dry fractures and faults (central part of Fig. 10D).

4.2.3. *Fracture kinematics and dilation*

A total of 258 piercing points along extension fractures were measured in the field (Figs. 11F and G) to distinguish the structures characterized by pure extension from those with a lateral component of opening. From a total of 39 structures, 11 have a right-lateral component, 12 are purely extensional and 14 have a left-lateral component. This strike-slip component is always very subordinate with respect to the component perpendicular to the average fracture strike. In fact, also from the rose diagram of Fig. 11D, it can be appreciated that on average the directions of opening are about perpendicular to the average fracture strike directions. Pure extensional fractures dominate in the central-southern part of the study area (Fig. 11B), whereas fractures with a left-lateral component dominate in the northern part (Fig. 11C). Despite the local complications in the kinematic pattern, vectors gradually rotate clockwise as fracture strikes also rotate clockwise (Fig. 11E). The

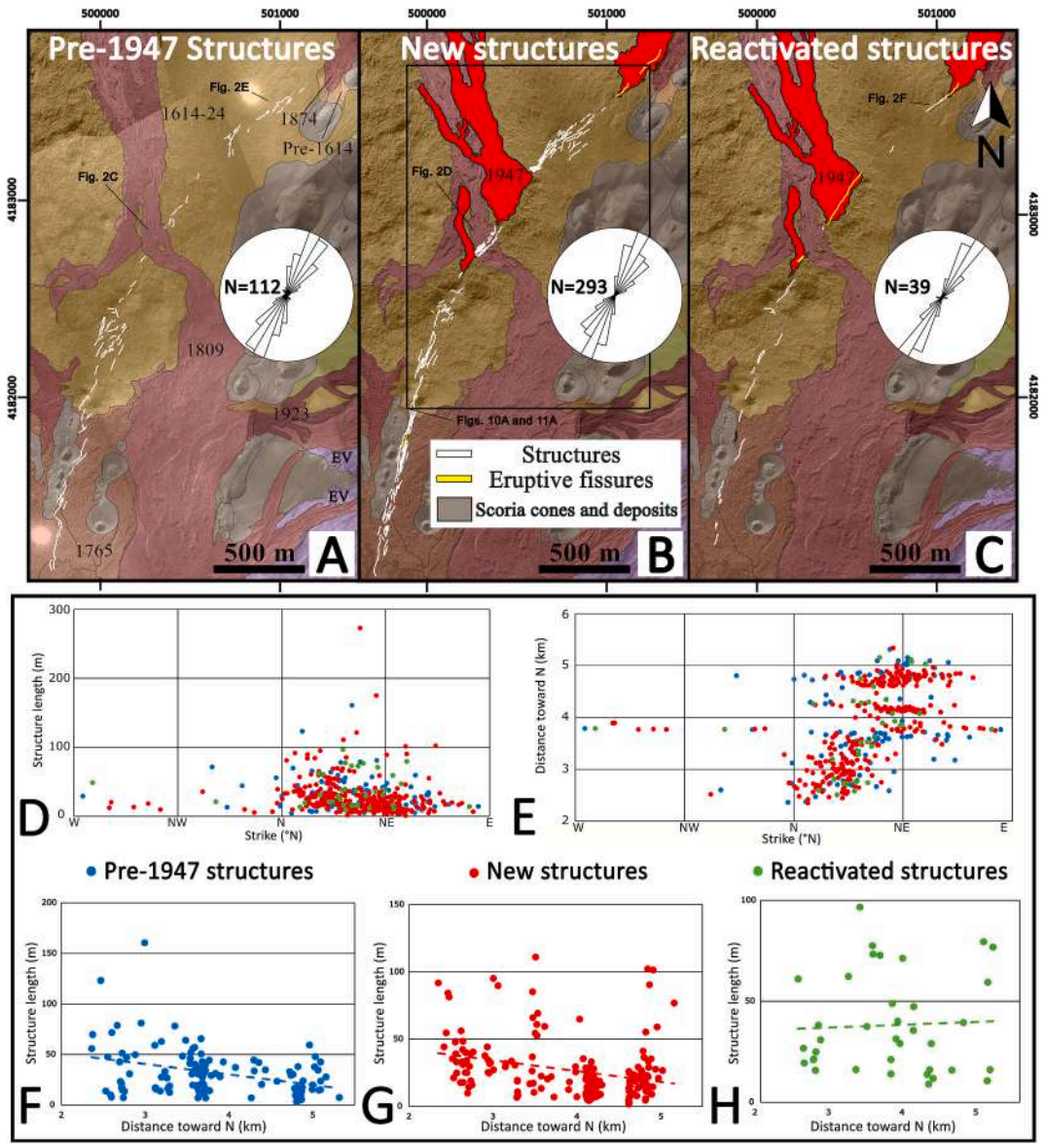

Fig. 9. Distribution of the mapped structures (A) from the 1932 OM and (B), (C) from the 1954 OM. Ages of historic lavas are shown. EV = Ellittico volcano lavas. The structures recognized in (C) were already present in 1932, but were reactivated in 1947. Rose diagrams show strike values for each category. (D) shows structure direction vs structure length, and (E) shows structure direction vs distance from the first point of eruption. (F), (G) and (H) show distance towards north vs structure length for (F) pre-existing structures, (G) new structures and (H) reactivated structures. Pre-existing structures are in blue, new structures are in red, and reactivated structures are in green dots. Reference system: UTM33-WGS84. (For interpretation of the references to colour in this figure legend, the reader is referred to the web version of this article.)

average vectors (large white arrows) in the southern, central, and northern parts of the studied area are shown in Fig. 11A, confirming the gradual clockwise rotation from south to north.

Along the opening vectors we also measured the opening amounts. These are represented as single points of measurement (black dots in Fig. 12A) with the dilation values expressed in a colour code. The values go from a minimum of 10 cm to a maximum of 1.3 m. There are two maxima in correspondence of the zones of vent opening. In the central zone of vent opening it was not possible to obtain values of dilation amount, due to lava flows that covered all the structures.

We also quantified the variations of dilation along the studied area (Fig. 12B). We considered a series of transects perpendicular to the local average orientation of the fracture swarm. To accurately capture the full extent of dyke-induced dilation still observable today, each transect was constructed as a 50-m-wide swath, within which we added the opening values of all the extension fractures affecting the transect, as well as the dilation component (heave) of the faults. Where the opening values of the faults were not clearly visible due to products filling or other reasons, the heave of the faults was calculated considering the vertical offset of the faults and a dip angle of 75°.

These accumulated opening amounts thus represent the total opening along the fracture swarm, and the graph gives the variations from south to north. Since it is impossible to measure the opening occurred prior to 1947 along the pre-existing fractures, the graph represents the combination of the opening occurred in 1947, and other possible deformation that took place since 1765 CE onwards. These data indicate that total dilation is mostly in the range of 2 to 5 m, with peaks in correspondence of the more developed grabens.

We also noticed that some of these dilation peaks are located in correspondence of local elevations. This part of the Etna flank is in fact constituted by a widespread lava field mostly produced by the 1614–1624 CE eruption, which shows a quite regular topography gently

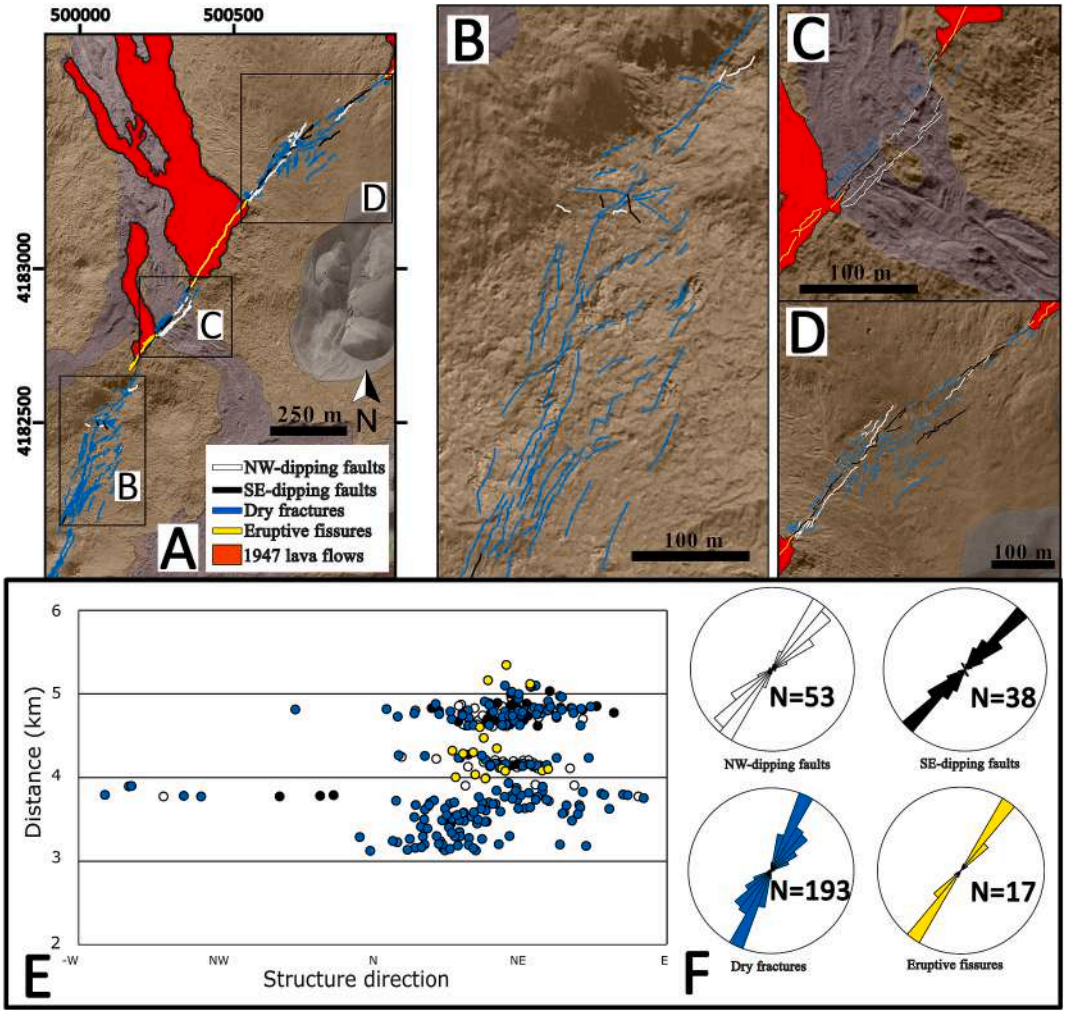

Fig. 10. (A) Map showing the structures, classified in NW- and SE-dipping faults, dry fractures and eruptive fissures induced by the 1947 event. The classification is made by field data collected in 2024 and by aerial historic photos. Location of this area is shown in Fig. 9B. (B), (C) and (D) show zoom in key areas. (E) Structure direction vs distance from the first point of eruption. Structures are classified as NW-dipping faults (white dots), SE-dipping faults (black dots), dry fractures (blue dots) and eruptive fissures (yellow dots). The respective rose diagrams are in (F). (For interpretation of the references to colour in this figure legend, the reader is referred to the web version of this article.)

sloping towards NE. Three elevated zones have been recognized along the 1947 swarm of structures, based on limited but evident local positive topography compared to the surrounding areas: Relief 1 to the south (C in Fig. 13), Relief 2 in the central part of the fracture swarm (A in Fig. 13), and Relief 3 in the northern part (B in Fig. 13, also indicated as "uplift" in Fig. 7H). Relief 1 and 2 are characterized by radial fractures, whereas Relief 3 has NE-SW fractures. These reliefs will be better discussed in Section 5.4.

4.2.4. *Fault slip profiles*

We collected 540 vertical offset values in the field (Fig. 4) and on UAV- derived images, along 102 faults of two grabens formed during the 1947 event (called Graben 2 and 3 in Fig. 14C). Among these faults, 29 were SE-dipping and 28 NW-dipping in Graben 2, and 31 SE-dipping and 14 NW-dipping in Graben 3. The cumulative vertical offset values allowed us to reconstruct the four slip profiles shown in Figs. 14 and 15 (SE- and NW-dipping for Graben 2, Fig. 14, and SE- and NW-dipping for Graben 3, Fig. 15).

All four slip profiles taper towards NE, i.e. the fault scarps height decreases from south to northeast. In Fig. 16 we show a couple of examples of 3D topographic models derived from UAV surveys. These models were reconstructed along the normal faults bounding Graben 2 and 3 (Fig. 15C). The fault scarps are well visible and show the highest vertical offset in the left part of the area, i.e. to the SW. The fault scarp height gradually decreases towards NE, tending to zero in the right part of the area, corresponding to the clear tapering of the fault slip profiles towards NE. A field picture of graben 3 is shown in Fig. 4A.

4.3. *Analogue models*

During the first phase of lateral intrusion, corresponding to a thickness of 3 mm in the model, a slight downwarping of the topographic surface started to appear. This downwarping was elongated in the same direction as the underlying dyke. Successive increments of thickness of the intrusion led to the formation of fractures, a few cm long, developed at the sides of the downwarping zone. Closer to the dyke source, fractures rapidly transform into normal faults (e.g. Figs. 17A-A'). These faults have scarps facing each other towards the dyke, giving rise to a graben. By gradually increasing the thickness of the intrusion, fracture length also increased in the same direction as dyke propagation, with linking between the various segments, or lengthening of already existing segments (e.g. Figs. 17B-B'). At the same time, during dyke thickening, already formed faults show an asymmetric increase of the scarp height, with higher throw where faults started to form, and decreasing throw in the same direction as dyke propagation.

Not all fracture segments linked together: some developed

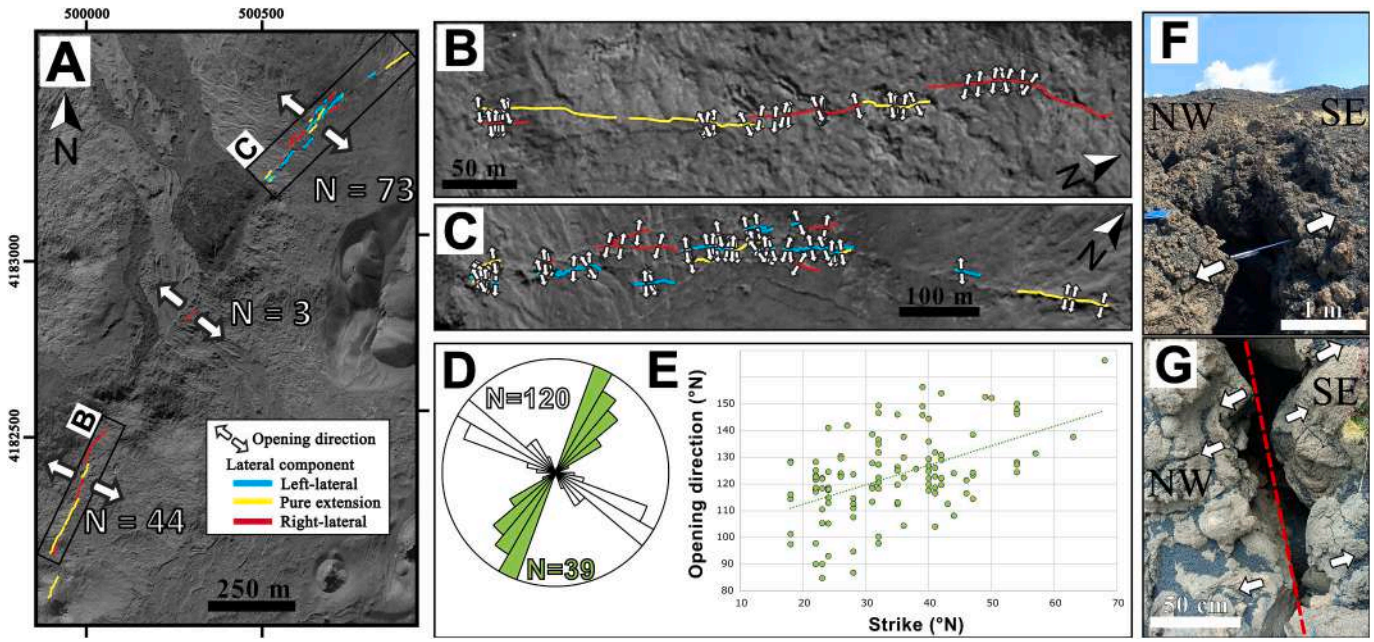

Fig. 11. (A) Map showing the structures classified in terms of their lateral component in left-lateral, pure extensional and right-lateral. The classification is made by field data collected in 2024. The area is the same of Fig. 10A. (B) and (C) represent a zoom in key areas. Vectors of fracture opening are provided as white arrows. (D) Rose diagram showing the strike of each classified structure (in green) and the opening direction (in white) at 120 piercing points collected on 39 structures. (E) Graph showing the relation between each structure's strike and each piercing point's opening direction. (F) and (G) show field examples of piercing points collected on different structures. In (G) the red line shows the strike of the structure. Reference system: UTM33-WGS84. (For interpretation of the references to colour in this figure legend, the reader is referred to the web version of this article.)

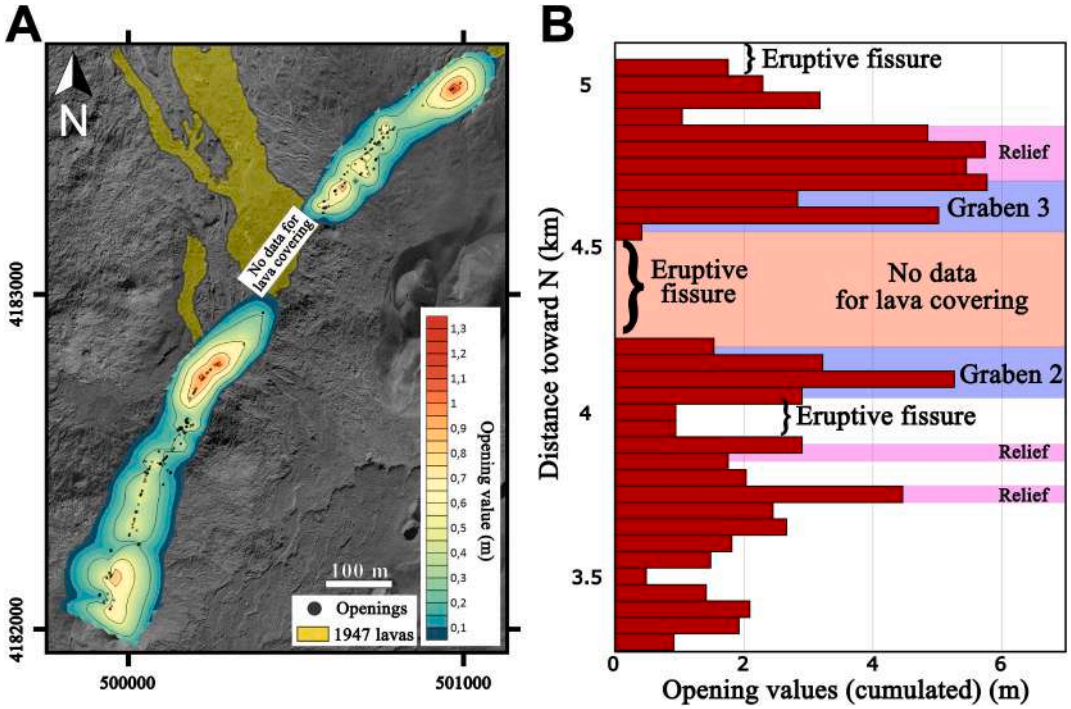

Fig. 12. (A) Contour lines of opening amounts measured at the same sites (black dots) of vector measurements of Fig. 11. Opening values range from 10 cm to 1.3 m. (B) Total dilation variations along the fracture zone, given as values of openings summed along a series of strips perpendicular to the average strike of the structures. The dataset is larger than that of Fig. 12A, considering more sites of measurements at extension fractures, and also the heave of normal faults. Dilation includes pre- and syn-1947 deformation, as well as possible post-1947 opening. Reference system: UTM33-WGS84.

independently. In the last phases of the experiments, some tips of the overlapping main fault segments started to bend towards the adjoining fracture, creating hooks. At the same time, during the last experiment phases, some fissures started to appear in the middle of the graben, above the ticker segment of the dyke (Figs. 17C-C' and 18 A). With further development of the structures, their length continuously increased mostly in the same direction of dyke propagation.

It is noteworthy that the graben shows a variation in width: the

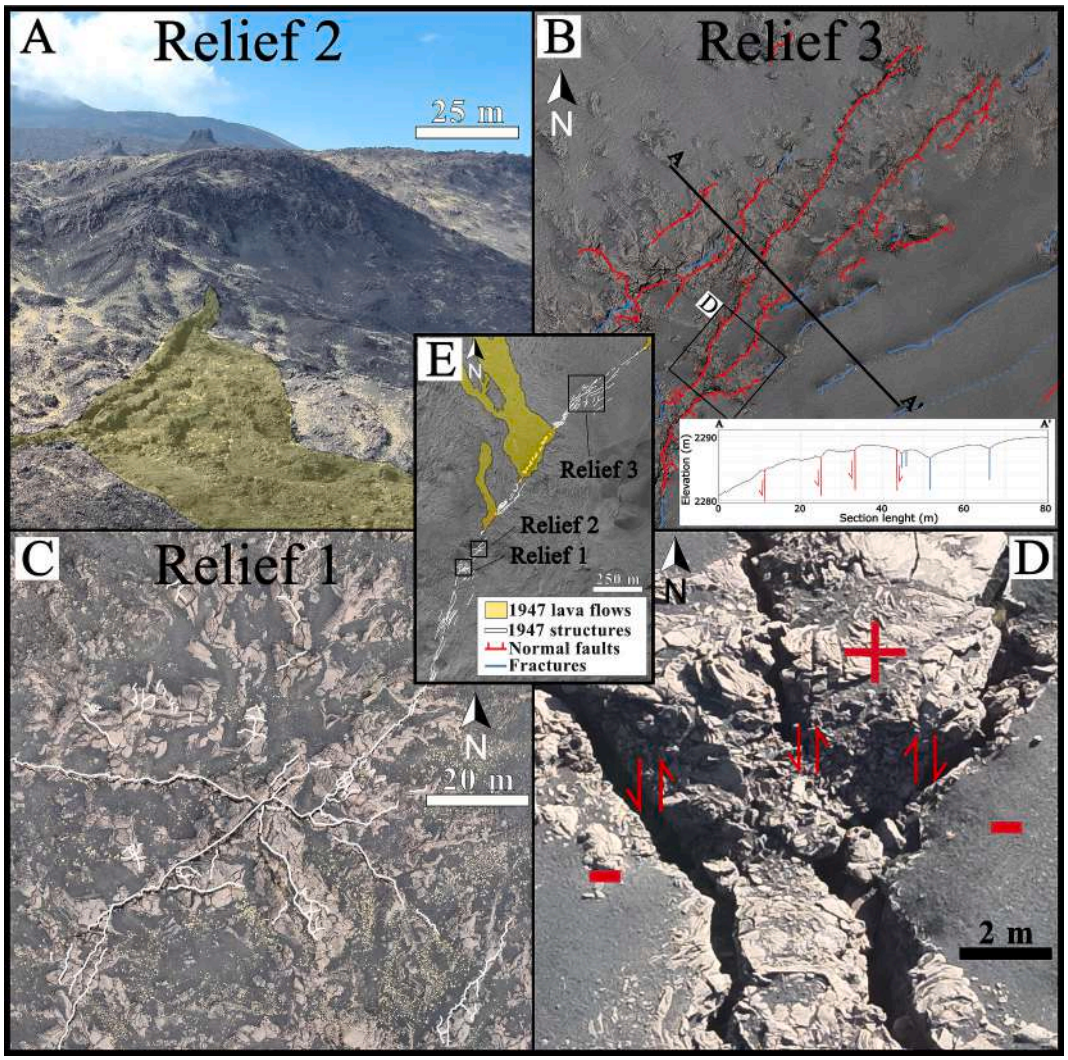

Fig. 13. (A) Drone oblique photo of relief zone 2 located in the southern part of the study area; (B) OM view of relief zone 3 located at the northernmost part of the 1947 fracture swarm, red lines are faults, blue lines are fissures, and topographic profile A-A' across the elevation; (C) OM view of relief zone 1, located in the southern part, with indication of the main radial fractures as white lines; (D) Detail of Relief 3 where the central block (+) is uplifted with respect to the sides (−). Red arrows show the relative block movements. (For interpretation of the references to colour in this figure legend, the reader is referred to the web version of this article.)

spacing between bounding faults decreases in the same direction as dyke propagation. This coincides with the direction of dyke thickness decrease, and as a consequence of the set-up of the apparatus, the decrease of graben width cannot be explained in terms of a deepening of the dyke tip.

At the end of the various experiments, using 3D models obtained by Structure from Motion, it has been possible to precisely measure the final throw along the fault scarps (e.g. in Figs. 18B and C). The maximum throws are opposite to the dyke propagation direction and range around 3 mm at both sides of the graben. The throws show some oscillation of about 1 mm, and gradually decrease in the same direction as dyke propagation down to zero. Throw values and the total length of the fracture system are very similar at both sides of the depression, indicating a graben symmetry. This reconstruction of the fault slip profiles clearly indicates the tapering of the fault scarps in the same direction as the longitudinal decrease of dyke thickness.

5. Discussion

5.1. Dyke propagation

The strong explosive activity that characterized the summit craters from February 5th to 16th 1947 produced a re-shaping of the crater morphology. The collapse into the vent of the inner walls of the crater can occur during cone growth, especially in association with pulses of magma ejection activity (Guest, 1973; Murray, 1980a, 1980b; Houghton and Schmincke, 1989; Calvari et al., 1998b; Falsaperla et al., 2005; Calvari and Pinkerton, 2004). Also the 600-m-high lava fountains that preceded the end of activity at the NEC and CC craters, might have contributed to the obstruction of the summit vents creating an obstacle to further magma vertical rise in the shallowest part of the main central conduit. Another possibility is that a transient decrease in magma contribution from the upper plumbing system resulted in debuttressing in the shallower conduit/vent. This, in turn, can trigger inward or vertical collapse of the summit cone, as observed at several active and inactive cinder cones (Guest et al., 1974; Houghton and Schmincke, 1989; Staudacher et al., 2009). In any case, the termination of volcanic activity at the summit craters was followed, after eight days, by the

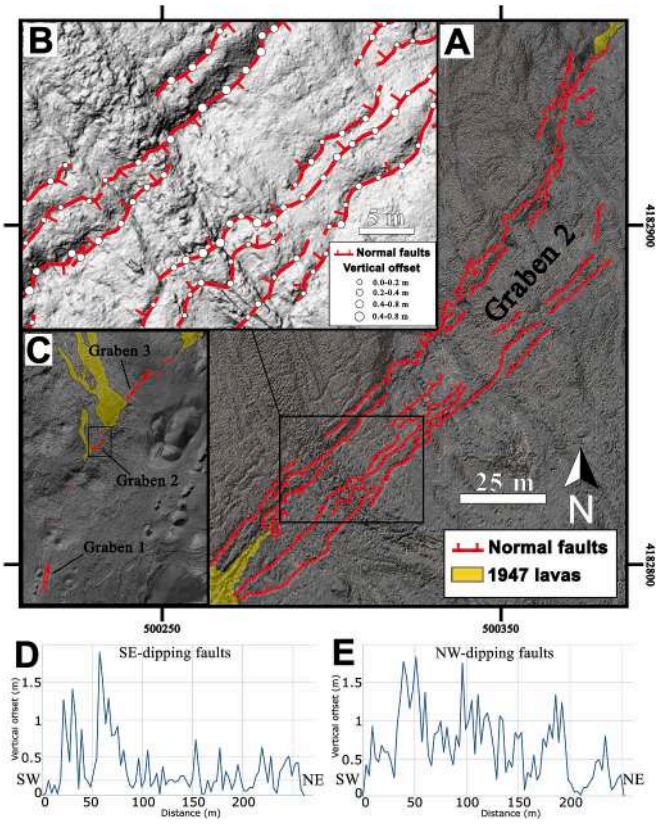

Fig. 14. (A) Map showing the normal faults of Graben 2 identified from the 2024 OMs and DEMs. The fault ticks indicate the lowered block. The background is a transparent OM overlapped on the shaded relief. (B) Detail from (A) where the vertical offsets of the normal faults are represented by white dots of proportional diameter. (C) Location of Graben 1, 2 and 3 (Graben 1 is now covered by more recent deposits). (D) and (E) show the slip profiles cumulated from all the SE- and NW-dipping faults, respectively. Vertical offsets were collected at a frequency of 3 m.

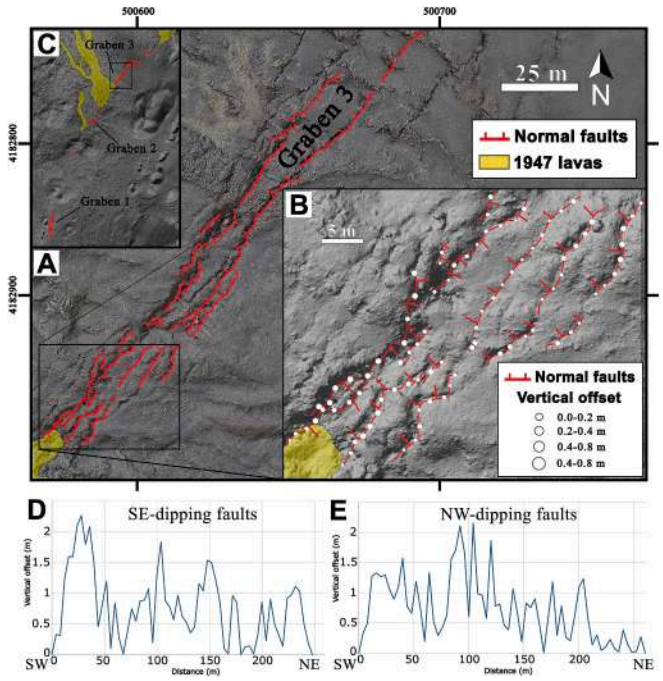

Fig. 15. (A) Map showing the normal faults of Graben 3 identified from the 2024 OMs and DEMs. The fault ticks indicate the lowered block. The background is a transparent OM overlapped on the shaded relief. (B) Detail from (A) where the vertical offsets of the normal faults are indicated with white dots of proportional diameter. (C) Location of Graben 1, 2 and 3 (graben 1 is now covered by more recent deposits). (D) and (E) show the cumulated slip profiles of all the SE- and NW-dipping faults, respectively. Vertical offsets were collected each 4 m. Reference system: UTM33-WGS84.

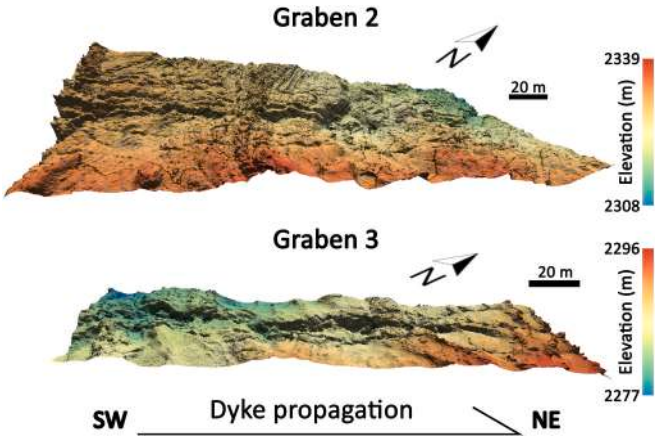

Fig. 16. 3D models obtained from UAV surveys and Structure from Motion elaboration. Location of Graben 2 and 3 in Fig. 15C. The tapering of the fault slip profiles towards NE is clearly visible.

initiation of opening of fractures and vents along the NE Rift (Silvestri, 1949). Later on, in a few hours the swarm of fractures propagated from the base of the NEC towards northeast for 6 km (Fig. 7). The development of these fractures was accompanied by the gradual opening of eruptive vents step-by-step, starting from an altitude of 3050 m (Vent 1 in Figs. 7 and 8). The successive vents 2, 3 and 4 opened in sequence towards the northeast at gradually decreasing altitudes.

This gradual propagation of the structures from higher to lower altitudes (i.e. from S to NE), including dry fractures and normal faults, as well as eruptive fissures and vents, is interpretable as the effect of the intersection between a laterally-propagating dyke, which originated from the main central conduit zone, and the volcano slope. The same interpretation was already made for other similar sequences of eruptions at Mt. Etna (Bousquet and Lanzafame, 2001) and Vesuvius (Acocella et al., 2006). If, on the contrary, the dyke propagated vertically, then the upper tip of the dyke would have intersected the slope of the volcano in the opposite sequence, i.e. uphill. The fact that a lava flow was fed for several days at the northeastern termination of the 1947 fracture swarm (Vent 4), indicates that the lateral flow of magma remained stable. Once activity at Vent 4 stopped, the new vents 6 and 7 opened at slightly higher altitudes. Magma eruption at these vents lowered the dyke overpressure, and, as a consequence, magma flow was no longer able to reach the same previous distance as far as vent 4. Instead, the formation of the northernmost topographic bulge on the night of February 27th (Silvestri, 1949), at 2150 m a.s.l., suggests that the stresses originated by the remaining overpressure were redirected upward. The upper dyke tip line (horizontal) was not able to propagate up to the surface, and thus magma must have locally accumulated in the subsurface, inducing upward deformation of the overburden.

5.2. Fault propagation

In order to understand the relationships between lateral dyke propagation and related shallow faulting, we focus on the slip profiles of the faults formed during the 1947 event. Slip profiles represent a proxy to record the cumulated displacement triggered during the phases of fault growth (Schlagenhauf et al., 2008). When a normal fault grows symmetrically, it extends the tips towards opposite directions (i.e. it grows in

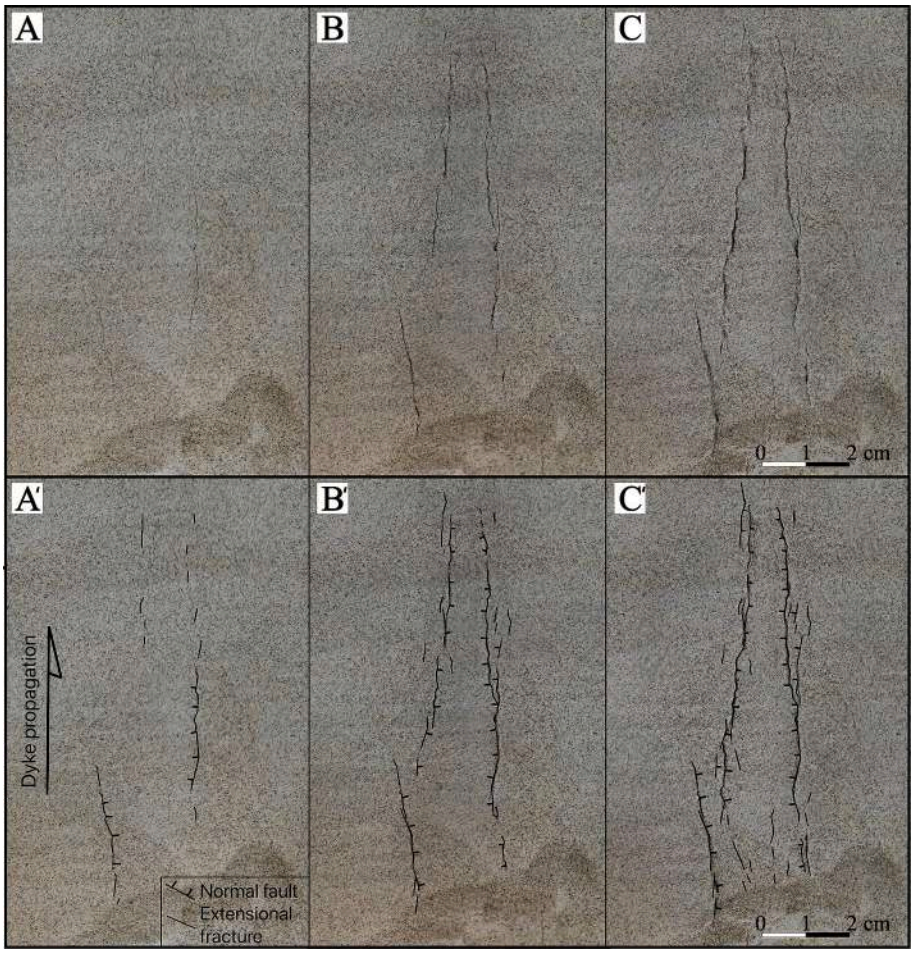

Fig. 17. Original photos (above) and interpretation (below) in plan view of examples of steps of development of analogue structures triggered by lateral dyke intrusion. In (A), first steps denote the formation of fractures and first faults at the sides of the downwarped area. In (B) previously formed fractures develop by segment linking and length increase; some extension fractures transform into normal faults. (C) Further development of structures by linkage; extension fractures appear in the middle of the previously formed grabens. Note that the overall lengthening of structures mostly occurs in the same direction of dyke propagation.

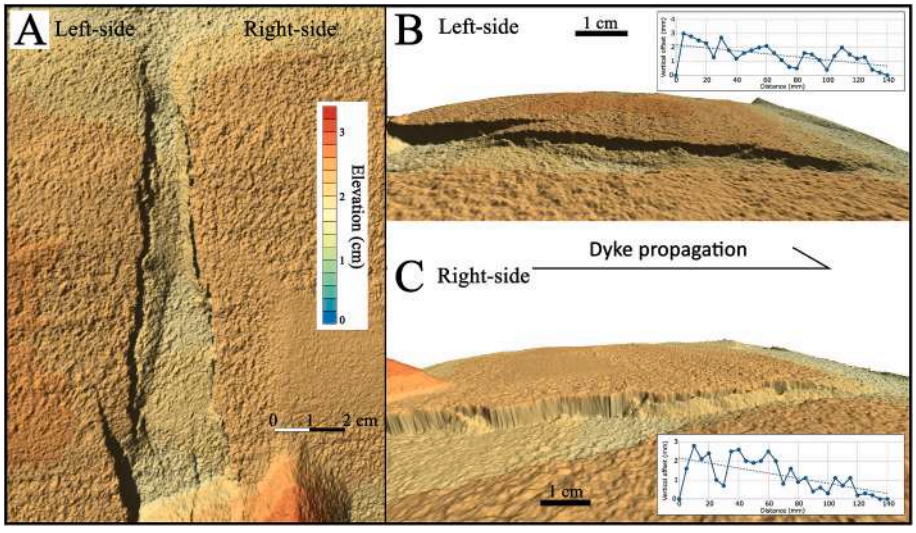

Fig. 18. 3D model of an analogue experiment, with the lateral propagation of the dyke at constant depth and thickness decrease in the same direction. (A) Aerial view of the graben formed during the experiment with the frontal views of the (B) left hand side and (C) right hand side of the graben. (B) and (C) also show the related fault slip profiles (and regression lines) for the left hand side of the graben and for its right hand side, respectively. The fault scarp tapering in the same direction of dyke propagation is very clearly noticeable. The vertical exaggeration of the 3D models is x1.6.

length) and increases the vertical offset towards the center of the fault trace (i.e. it grows vertically) (Tentler and Mazzoli, 2005). This corresponds to an elliptical fault slip profile, where the maximum slip is at the center of the fault, which tapers outwards at both ends (Pollard and Segall, 1987; Cowie and Scholz, 1992; Scholz, 2002). Instead, an asymmetric slip profile represents the combination of fault vertical growth and unidirectional propagation of the slip plane (Nicol et al., 1996; Manighetti et al., 2001, 2004; Roche et al., 2012; Tibaldi et al., 2019).

Specifically, regarding the relationship between dyke injection and related fault propagation, there is a general lack of data in the literature in terms of fault tapering. Tibaldi et al. (2020c) described the normal faults that fade into extension fractures in the same direction of dyke propagation, during the Krafla Fires (1975–1984), in Iceland. This should correspond to tapering of the graben faults in the same direction. Ruch et al. (2016) documented the formation of a graben during the Barðarbunga (Iceland) volcanotectonic event in 2014. Values of subsidence along the grabens formed during this event decrease northwards, consistently with the dyke propagation in the same direction (Sigmundsson et al., 2015). Only in very recent times, some research started to be carried out to systematically measure fault slip profiles linked to surface deformations triggered by dyke intrusions (Tibaldi et al., 2016, 2019, 2020b; Dumont et al., 2017), showing that normal faults dominantly taper outwards from a magma chamber, which is to say in the same direction of dyke lateral propagation. However, most of these research efforts, apart from Bardarbunga, do not rely on independent data on the effective lateral dyke propagation coeval with the propagation of a given fault.

In the present work, the analysis of slip profiles of faults formed contemporaneously to the lateral propagation of the 1947 dyke shows that the maximum throw occurred towards the source of the dyke (i.e. towards the central conduit zone). Based also on Dawers and Anders (1995) and Kattenhorn and Pollard (2001), the location of maximum throw represents the area where the fault nucleated. Towards NE (i.e. outward from the volcano), the average throw decreases, although several irregularities can be recognized. The irregularities where throw reduction occurs, indicate sites of fracture segment linkage (Walsh et al., 2003). The northeastward tapering of slip profiles thus coincides with the direction of lateral propagation of the 1947 dyke. Although asymmetric slip profiles have been previously attributed to mechanical interaction between fault segments (Willemse, 1997; Maerten et al., 1999), we point out that this interpretation regarded faults triggered by tectonic activity. Based on our data, instead, it is possible to explain the tapering of dyke-induced normal faults as influenced by the lateral propagation of a shallow dyke. This pattern would differ if the dyke propagated vertically, as occurred, for example, in the 2001 Mt. Etna eruption (Acocella and Neri, 2003). In this case, fracture propagation would depend on the angle between the upper tip of the dyke and the volcano flank slope. Specifically, if the upper tip of the dyke was mostly horizontal (the most plausible case for an upward rising dyke), forming an angle with the volcano slope, the dyke-triggered fracture would propagate uphill, opposite to what is observed in our data. If instead the upper tip of the dyke was parallel to the slope, the resulting fractures would not exhibit any preferential propagation direction.

These field data can be compared in synergy with our analogue models. Scaled physical models on fault tapering are very limited in the literature. While several analogue models have already been carried out to analyze the general development of normal faults (e.g. Horsfield, 1977; Ackermann et al., 2001; Mansfield and Cartwright, 2001; Bellahsen et al., 2003; Marchal et al., 2003; Bellahsen and Daniel, 2005; see also references in Zwaan and Schreurs, 2022), specific modelling of slip profiles has been conducted only by Schlagenhauf et al. (2008), as far as we know. This modelling has been devoted to reproducing normal faults development under a homogenous far-field tectonic stress field. Instead, our analogue models mimic lateral dyke propagation and related fault slip profile development. During the increase of dyke thickness, we observed the i) gradual lengthening of the faults and ii) increase of fault scarps. i) The increase of length is consistent with the historical field data, which indicates that the propagation of the structures evolved. It was observed, for example, that the fissure located 2300 m a.s.l. had a length of 36 m on February 24th, which increased up to 138 m after two days, and then to 325 m on March 5th. ii) In regard to the increase of fault scarps, the fault throw in the experiments became gradually larger, especially at the fault tip opposite to the direction of dyke propagation. At the end of each experiment, the maximum throw was located near one tip of the fault. In the opposite direction, i.e. towards the dyke propagation, the cumulated offset was gradually less, resulting in a clear tapering in the same direction. In our experiments, this tapering thus corresponds to a decrease of dyke thickness with distance from the source. In the 1947 event, the tapering of the faults bounding the grabens might correspond to a decrease of dyke thickness with distance from the central conduit zone. The various pulses of magma intrusions that accompanied the formation of the various vents and fed the huge lava flows could have been logically accompanied by the gradual thickening of the dyke. With distance from the source zone, the overpressure in fact decreases with the consequent thinning of the dyke. Since surface deformation is proportional to the stresses transmitted by the dyke tip, the decrease of thickness/overpressure with distance corresponds to a decrease of surface deformations, i.e. fault offset.

5.3. *Pre-existing fractures vs new fracture arrangement*

We showed that the 1947 dyke intrusion followed exactly the curved trace of a swarm of pre-existing fractures (Figs. 9A-C). Due to the typical volcanotectonic activity of the NE Rift, it is very likely that the swarm of pre-existing structures was induced by a previous dyke intrusion. Based on the crosscutting relationships between the fractures and the ages of lava deposits, this event can be dated between 1614 and 1624 and 1809 CE. Considering the distribution in time and space of the various historical events on the northern Etna flank, the fracture swarm may have formed during the latest phases of the 1614–1624 long eruption, or during the 1764–65 CE event. It is very well known that pre-existing discontinuities in the host rock may channelize dykes, possibly inducing their arrest or deviation (Gudmundsson, 1983, 1986; Delaney et al., 1986; Rossetti et al., 2000; Ziv et al., 2000; Ito and Martel, 2002; Watanabe et al., 2002; Valentine and Krogh, 2006; Mathieu et al., 2008; Bonali et al., 2012; Le Corvec et al., 2013; Maccaferri et al., 2016; Spacapan et al., 2016; Swanson et al., 2019; Thiele et al., 2021; Greiner et al., 2023; Mannini et al., 2024). Whether a dyke follows a fault as a path for magma propagation, depends mainly on the angle between the dyke and the fracture, and on the ratio between the tensile strength of the host rock and the tensile strength across the fault (Drymoni et al., 2021; Gudmundsson, 2022). The greater probability for a fracture to act as a magma path occurs if: *i)* the fracture is steeply dipping, *ii)* with close to zero tensile strength, and *iii)* the surrounding stress regime is extensional (Ziv et al., 2000; Gudmundsson, 2022).

In the case of the NE Rift, our data are consistent with the previous assumptions; regarding point *i)*, the rectilinear trace of the various fracture segments suggests that they are steeply dipping. For point *ii)*, having the fractures a historic age, there has not been enough time for the development of sealing processes (Knipe, 1992), thus the tensile strength across the fractures should be very low or equal to zero. For point *iii)*, the general stress regime along the NE Rift and in the surrounding rock volumes is extensional, with a horizontal least principal stress σ_3 trending from WNW-ESE to NW-SE (Tibaldi et al., 2021). This regime is mainly due to the tension forces exerted by the eastward gravity slip of the eastern flank of Mt. Etna (Apuani et al., 2013; Urlaub et al., 2018). The slip occurs at a few cm per year, with a sliding sector bounded by the left-lateral transtensional Pernicana Fault to the north, and by the NE Rift and S Rift to the west (Fig. 1B) (Borgia et al., 1992; Rust and Neri, 1996; Tibaldi and Groppelli, 2002). By comparing the general regime in this sector of Mt. Etna, with the direction and amount

of opening of the 1947 structures, we are aware that these last ones might result from the superimposition of pre-1947 deformation on successive deformation. Anyway, since most of the structures here formed during 1947, the measured data should give a gross estimation of the kinematics of that event. The gradual rotation of the opening vectors measured along the 1947 fracture swarm, denotes a dominant pure dilation. Dilation vectors are oriented as the maximum slope gradient of this sector of Mt. Etna. We thus consider the location and structural characteristics of the 1947 event as affected also by the extensional processes that gradually lower the σ_3 in the surrounding rocks, as also observed, for example, at Newberry volcano in the Cascades (Beachly et al., 2012), or at Kīlauea volcano, Hawai'i, where the instability of volcano flanks can reduce the stress normal to a volcanotectonic rift (e.g. Fig. S1 in Montgomery-Brown and Miklius, 2021).

The pre-existence of a fracture swarm along the path of the 1947 dyke can also explain the high dyke propagation rate, in the order of 6 km in a few hours; the dense network of suitably-oriented tangential fractures offered a more permeable pathway for magma transport. This is similar to the time period of a few hours necessary for repeated intrusions, which led to flank eruptions along rift-fractured zones at Piton de La Fournaise volcano (La Reunion) from 2000 to 2003, and corresponding to lateral migration speeds of the dyke ranging between 0.2 m/s and 0.8 m/s (Peltier et al., 2005).

35 % of the pre-existing fractures were reactivated by the 1947 dyke intrusion, with a significant increase of length, and ten were reactivated as eruptive fissures. The comparison between the location of pre-, *syn*-, and reactivated 1947 structures, suggests that the stresses transmitted upward by dyke overpressure were dissipated by formation of the new mechanical discontinuities, or by the lengthening of existing ones, but the coexistence of both process in the same site was uncommon. Moreover, the gradual decrease of length of pre-1947 and syn-1947 fractures towards northeast, could be the effect of a decrease of magma overpressure with distance from the source of the dyke during lateral magma flow. It is also noteworthy that all the vents formed in correspondence of pre-existing fractures, consistent with the necessity of minor energy for a magma pathway along a suitably-oriented discontinuity with zero tensile strength (Gudmundsson, 2022).

Regarding the large number of pre-existing fractures that were not reactivated, we can speculate that this might depend upon the balance between magma overpressure and the distance between the fracture and the new dyke. The stresses transmitted by dyke overpressure of course decreases with distance and thus it is possible that beyond a critical range, these stresses are not enough to further develop the already existing rock discontinuities. However, other parameters can influence this process, such as mechanical properties of the fractures and surrounding rocks, orientation of the pre-existing fracture with respect to the dyke, etc., and we suggest that further studies are needed to better understand this issue.

5.4. *Elevations and segmentation of lateral magma propagation*

The elevations named Relief 1 and 2, show a large range of fracture strikes with a radial pattern. These elevations are made of lavas dated to 1614–1624 CE with a radial pattern of short lava flows outpoured from the summit zone of the relief. This indicates that these elevations existed prior to the 1947 event and were considered as megatumuli by Guest et al. (1984b). The first step of formation of the local radial fracture pattern can have been induced by the inner growth of the megatumuli during the 1614–1624 event, accompanied by short lava flows emitted through these fractures. Anyway, at the same two elevations we observed, with the historical aerial photos, the formation of some new radial fractures and elongation of pre-existing fractures during the 1947 event. During magma-induced doming, in fact, radial fractures can develop (Luongo et al., 1991; Montanari et al., 2017), and more specifically dykes can produce local uplift (Gudmundsson et al., 2008; Abdelmalak et al., 2012). The fact that these two zones of radial fracturing further developed during the 1947 eruption suggests that they might correspond to upward-directed push from a local magma stalling in the dyke. These two reliefs also coincide with a change in the general strike of both the pre-1947 and 1947 fracture swarm. All these characteristics are similar to the data collected during the 2014 Barðarbunga event (Iceland), when the lateral dyke propagation developed by segmentation with a change in dyke strike and transient arrest in correspondence of topographic elevations (Sigmundsson et al., 2015). This was interpreted as due to larger lithostatic pressure that acted as barriers to magma lateral propagation.

We suggest that further investigations should be necessary to assess if similarly, in the case of the 1947 event, the megatumuli elevations could have acted as topographic/lithostatic barriers. Considering the width of the 1947 grabens outside these two elevations, following the rule that relates the depth of the dyke tip to the width of the dyke-induced graben as ½ ratio (Pollard et al., 1983; Mastin and Pollard, 1988; Trippanera et al., 2015), our data suggest possible depth variations of the upper dyke tip mostly in the range of a few meters to 13 m, up to local maximum of 50 m. Although this rule cannot always be precise (Magee and Jackson, 2021), the dyke tip was anyway very shallow, whereas in correspondence of the two elevations, the topography adds a relief in the order of 50–100 m. In the hypothesis, to be verified, that megatumuli may have acted as barriers, lateral dyke propagation may have been slowed or arrested, with a transient buildup of overpressure. This could have first induced radial fractures in the overburden and then, once the pressure in the dyke reached an adequate threshold, the formation of a new dyke segment, with a change in strike, which lengthened the overall intrusion. Further studies on this important topic should also take into account that barriers at laterally-propagating dykes, cannot be due only to variations in lithostatic pressure (Maccaferri et al., 2011; Sigmundsson et al., 2015), but also to lateral changes in rock mechanical properties (e.g. lateral changes of lithology), or to the presence of concealed structures (similar to the stress barriers, as shown by Gudmundsson, 2003).

Regarding Relief 3, its faults formed during the 1947 event. The fact that they depict a NE-SW swarm, instead of a radial pattern, suggests that they first formed as a graben, and then the upward magma push inverted the normal faults as reverse shear zones, similarly to what was observed in Iceland by Gudmundsson et al. (2008). Based on this author, the uplifted area bounded by reverse faults is due to the upward stress transmission above the dyke. Based on Abdelmalak et al. (2012), the formation of uplift with reverse faults can also be due to the dyke tip that interacts with fractures formed during a previous stage; the dyke is deflected from its vertical trajectory and propagates towards the surface along one of these fractures inducing surface uplift.

6. Conclusions

We provided a detailed analysis of the volcanotectonic structures formed during the 1947 Mt. Etna lateral eruption and in previous times, along the NE Rift, based on historical accounts and aerial photos, archival images, and contemporary field and drone data. The main results include:

- The progressive time evolution of the volcanic vents, eruptive fissures and the other structures deduced from historical chronicles, indicates that the 1947 event was due to the lateral NE-ward propagation of a shallow dyke.
- We classified 301 structures, 90 of which are normal faults (53 NW-dipping and 37 SE-dipping), 194 are dry fractures and 17 are eruptive fissures. The fractures form a swarm with a N-S trend in the southern part, to a NE-SW trend in the northern part, for a total length of 6 km.
- In the same swarm, we classified 112 structures to have an age corresponding to the ending of the 1614–24 CE eruption or to the 1764–65 CE eruption, and 293 structures formed during the 1947

event. The 1947 dyke reactivated 39 structures, corresponding to 35 % of the total pre-existing fractures in the area, with a significant increase of their length. Ten structures were reactivated as eruptive fissures, generating vents and lava flows.

- A total of 258 piercing points along extension fractures were measured to quantify the opening vectors. Pure dilation was dominant along most of the fracture swarm. These vectors are parallel to the general slope of Mt. Etna and are consistent with the gravity effect linked to the eastward sliding of the volcano flank. Total dilation measured along the fracture swarm is in the range of 2 to 5 m.
- Slip profiles measured along the main 1947 faults taper towards NE, i.e. the fault scarps height decreases downhill. Analogue models have also been carried out to simulate how lateral magma propagation and dyke thickness variation can influence fault slip profiles.
- There are two elevated areas along the fracture zone which show radial fracture patterns. These patterns were present at pre-1947 times, and were further developed during 1947. A third relief zone instead shows a NE-SW horst, parallel to the general fracture swarm.
- Our data suggest that at a central volcano, magma upwelling focuses at the central conduit zone, but the possible closure of the summit vent, accompanied by predisposing factors in the surrounding rocks, can facilitate lateral magma propagation. These predisposing factors are mainly represented by a possible slip of the volcano flank that brings compressive stresses at a minimum, the overpressures generated by replenishment of the shallow magma plumbing system, and the pre-existence of cracks along a rift.
- The fluid propagates laterally along the pre-existing fracture swarm, but the overpressure can also actively force the outward injection of magma along new hydrofractures. Thus, the lateral magma flow may be viewed as both a passive mechanism that exploits pre-existing discontinuities, as well as a driving mechanism for the contemporaneous formation of new fissures and fault swarms. Normal faults can develop asymmetric slip profiles, which taper in the same direction of the lateral dyke propagation.
- The hypothesis that lateral dyke propagation can be stopped by barriers such as topographic elevations of the order of megatumuli, is worth being more deeply investigated. In this case, magma, pushing upwards, can lead to the formation of radial fractures, until the pressure reaches again a threshold that allows the elevation barrier to be overcome and the dyke to be extended.

We wish to stress that the great deal of data presented here may represent a valuable and stimulating basis for conducting further research, including analogue and numerical modelling, aimed at shedding more light on lateral dyke propagation processes and the role of pre-existing fractures.

CRediT authorship contribution statement

A. Tibaldi: Writing – review & editing, Writing – original draft, Supervision, Funding acquisition, Conceptualization. **A. Luppino:** Writing – review & editing, Writing – original draft, Investigation, Formal analysis, Data curation. **E. De Beni:** Writing – review & editing, Investigation. **N. Corti:** Writing – review & editing. **M. Cantarero:** Investigation. **F. Pasquarè Mariotto:** Writing – review & editing. **F.L. Bonali:** Writing – review & editing, Supervision, Investigation, Data curation.

Declaration of competing interest

The authors declare that they have no known competing financial interests or personal relationships that could have appeared to influence the work reported in this paper.

Acknowledgments

We acknowledge two anonymous referees that greatly helped to improve a previous version of the manuscript. We also acknowledge Catania's Biblioteche Riunite Civica and A. Ursino Recupero and Linguaglossa's A. Gullo libraries for consulting historical texts. The authors are grateful to the INGV-OE staff which manages the Sicili@net. This work was supported by funding provided by the Italian Presidenza del Consiglio dei Ministri - Dipartimento della Protezione Civile (DPC), Convenzione Attuativa A. This paper does not necessarily represent DPC official opinion and policies. Further funding was provided by the International Lithosphere Program, Task Force II. This paper is also an outcome of the Virtual Reality lab for Earth Sciences - GeoVires (https://geovires.unimib.it/), University of Milano-Bicocca. Agisoft Metashape is acknowledged for photogrammetry processing.

Data availability

Data will be made available on request.

References

Abdelmalak, M.M., Mourgues, R., Galland, O., Bureau, D., 2012. Fracture mode analysis and related surface deformation during dyke intrusion: Results from 2D experimental modelling. Earth Planet. Sci. Lett. 359, 93–105.

Ackermann, R.V., Schlische, R.W., Withjack, M.O., 2001. The geometric and statistical evolution of normal fault systems: an experimental study of the effects of mechanical layer thickness on scaling laws. J. Struct. Geol. 23, 1803–1819.

Acocella, V., 2021. Volcano-Tectonic Processes, Advances in Volcanology. Springer Nature, Switzerland.

Acocella, V., Neri, M., 2003. What makes flank eruptions? The 2001 Etna eruption and its possible triggering mechanisms. Bull. Volcanol. 65, 517–529.

Acocella, V., Neri, M., 2009. Dike propagation in volcanic edifices: overview and possible developments. Tectonophysics 471 (1–2), 67–77.

Acocella, V., Porreca, M., Neri, M., Mattei, M., Funiciello, R., 2006. Fissure eruptions at Mount Vesuvius (Italy): insights on the shallow propagation of dikes at volcanoes. Geology 34, 673–676. https://doi.org/10.1130/G22552.1.

Acocella, V., Neri, M., Sulpizio, R., 2009. Dike propagation within active central volcanic edifices: constraints from Somma-Vesuvius, Etna and analogue models. Bull. Volcanol. 71, 219–223. https://doi.org/10.1007/s00445-008-0258-2.

Acocella, V., Neri, M., Norini, G., 2013. An overview of experimental models to understand a complex volcanic instability: Application to Mount Etna, Italy. J. Volcanol. Geotherm. Res. 251, 98–111.

Ágústsdóttir, T., Woods, J., Greenfield, T., Green, R.G., White, R.S., Winder, T., Brandsdóttir, B., Steinthórsson, S., Soosalu, H., 2016. Strike-slip faulting during the 2014 Bárðarbunga-Holuhraun dike intrusion, central Iceland. Geophys. Res. Lett. 43 (4), 1495–1503.

Anderson, E.M., 1951. Dynamics of faulting and dyke formation, 2nd edn. Olivier and Boyd, Edinburgh.

Antoniou, V., Bonali, F.L., Nomikou, P., Tibaldi, A., Melissinos, P., Mariotto, F.P., Vitello, F.R., Krokos, M., Whitworth, M., 2020. Integrating virtual reality and GIS tools for geological mapping, data collection and analysis: An example from the Metaxa mine, Santorini (Greece). Appl. Sci. 10 (23), 8317.

Apuani, T., Corazzato, C., Merri, A., Tibaldi, A., 2013. Understanding Etna flank instability through numerical models. J. Volcanol. Geotherm. Res. 251, 112–126.

Azzaro, R., Branca, S., Gwinner, K., Coltelli, M., 2012. The volcano-tectonic map of Etna volcano, 1: 100.000 scale: an integrated approach based on a morphotectonic analysis from high-resolution DEM constrained by geologic, active faulting and seismotectonic data. Ital. J. Geosci. 131 (1), 153–170.

Bagnardi, M., Amelung, F., Poland, M.P., 2013. A new model for the growth of basaltic shields based on deformation of Fernandina volcano, Galápagos Islands. Earth Planet. Sci. Lett. 377, 358–366.

Barreca, G., Bonforte, A., Neri, M., 2013. A pilot GIS database of active faults of Mt. Etna (Sicily): A tool for integrated hazard evaluation. J. Volcanol. Geotherm. Res. 251, 170–186.

Bates, R., Jackson, J.A., 1987. Glossary of Geology, 3rd edition. McGraw-Hill Book Company. (788 pp.).

Battaglia, M., Di Bari, M., Acocella, V., Neri, M., 2011. Dike emplacement and flank instability at Mount Etna: constraints from a poro-elastic-model of flank collapse. J. Volcanol. Geotherm. Res. 199 (1–2), 153–164.

Beachly, M.W., Hooft, E.E., Toomey, D.R., Waite, G.P., 2012. Upper crustal structure of Newberry volcano from P-wave tomography and finite difference waveform modeling. J. Geophys. Res. Solid Earth 117 (B10).

Bellahsen, N., Daniel, J.M., 2005. Fault reactivation control on normal fault growth: an experimental study. J. Struct. Geol. 27, 769–780.

Bellahsen, N., Daniel, J.M., Bollinger, L., Burov, E., 2003. Influence of viscous layers on the growth of normal faults: insights from experimental and numerical models. J. Struct. Geol. 25, 1471–1485.

Bonaccorso, A., Branca, S., 2010. Fotografia storica alla luce del vulcano. *Fondo Fotografico Gaetano Ponte (1876-1955)*. Le Nove Muse, Catania.
Bonali, F.L., Corazzato, C., Tibaldi, A., 2012. Elastic stress interaction between faulting and volcanism in the Olacapato–San Antonio de Los Cobres area (Puna plateau, Argentina). Glob. Planet. Chang. 90, 104–120.
Bonali, F.L., Tibaldi, A., Corazzato, C., 2015. Sensitivity analysis of earthquake-induced static stress changes on volcanoes: the 2010 M w 8.8 Chile earthquake. Geophys. J. Int. 201 (3), 1868–1890.
Bonali, F.L., Tibaldi, A., Mariotto, F.P., Russo, E., 2018. Interplay between inherited rift faults and strike-slip structures: Insights from analogue models and field data from Iceland. Glob. Planet. Chang. 171, 88–109.
Bonali, F.L., Tibaldi, A., Marchese, F., Fallati, L., Russo, E., Corselli, C., Savini, A., 2019. UAV-based surveying in volcano-tectonics: An example from the Iceland rift. J. Struct. Geol. 121, 46–64.
Bonali, F.L., Corti, N., Mariotto, F.P., De Beni, E., Bressan, S., Cantarero, M., Russo, E., Neri, M., Tibaldi, A., 2024a. 3D study of dyke-induced asymmetric graben: The 1971 Mt. Etna (Italy) case by structural data and numerical modelling. J. Struct. Geol. 187, 105231.
Bonali, F.L., Vitello, F., Kearl, M., Tibaldi, A., Whitworth, M., Antoniou, V., Russo, E., Delage, M., Nomikou, P., Becciani, U., van Wyk de Vries, B., Krokos, M., 2024b. GeaVR: An open-source tools package for geological-structural exploration and data collection using immersive virtual reality. Appl. Comput. Geosci. 21, 100156.
Bonforte, A., Gambino, S., Neri, M., 2009. Intrusion of eccentric dikes: the case of the 2001 eruption and its role in the dynamics of Mt. Etna volcano. Tectonophysics 471 (1–2), 78–86.
Borgia, A., Ferrari, L., Pasquarè, G., 1992. Importance of gravitational spreading in the tectonic and volcanic evolution of Mount Etna. Nature 357 (6375), 231–235.
Bousquet, J.C., Lanzafame, G., 2001. Nouvelle interprétation des fractures des éruptions latérales de l'Etna: Conséquences pour son cadre tectonique. Bull. Soc. Geol. Fr. 172, 455–467.
Branca, S., Del Carlo, P., 2004. Eruptions of Mt Etna during the past 3.200 years: a revised compilation integrating the Historical and stratigraphic records. Mt. Etna: volcano laboratory.
Branca, S., Del Carlo, P., 2005. Types of eruptions of Etna volcano AD 1670–2003: implications for short-term eruptive behaviour. Bull. Volcanol. 67, 732–742.
Branca, S., Coltelli, M., De Beni, E., Wijbrans, J., 2008. Geological evolution of Mount Etna volcano (Italy) from earliest products until the first central volcanism (between 500 and 100 ka ago) inferred from geochronological and stratigraphic data. Int. J. Earth Sci. 97, 135–152.
Branca, S., Coltelli, M., Groppelli, G., 2011a. Geological evolution of a complex basaltic stratovolcano: Mount Etna, Italy. Ital. J. Geosci. 130 (3), 306–317.
Branca, S., Coltelli, M., Groppelli, G., Lentini, F., 2011b. Geological map of Etna volcano, 1: 50,000 scale. Ital. J. Geosci. 130 (3), 265–291.
Calvari, S., Pinkerton, H., 2004. Birth, growth and morphologic evolution of the 'Laghetto'cinder cone during the 2001 Etna eruption. J. Volcanol. Geotherm. Res. 132 (2–3), 225–239.
Calvari, S., Tanner, L.H., Groppelli, G., 1998a. Debris-avalanche deposits of the Milo Lahar sequence and the opening of the Valle del Bove on Etna volcano (Italy). J. Volcanol. Geotherm. Res. 87 (1–4), 193–209.
Calvari, S., Müller, W., Scribano, V., 1998b. Eruptive activity and morphology evolution of Bocca Nuova, one of the four of Etna's summit craters, from 1988 to 1995. Acta Vulcanol. 10, 27–31.
Calvari, S., Tanner, L.H., Groppelli, G., Norini, G., 2004. Valle del Bove, eastern flank of Etna volcano: a comprehensive model for the opening of the depression and implications for future hazards. In: Etna Volcano Laboratory. American Geophysical Union.
Cannata, A., Iozzia, A., Alparone, S., Bonforte, A., Cannavò, F., Cesca, S., Gresta, S., Rivalta, E., Ursino, A., 2021. Repeating earthquakes and ground deformation reveal the structure and triggering mechanisms of the Pernicana fault, Mt. Etna. Commun. Earth Environ. 2 (1), 116.
Cappello, A., Neri, M., Acocella, V., Gallo, G., Vicari, A., Del Negro, C., 2012. Spatial vent opening probability map of Etna volcano (Sicily, Italy). Bull. Volcanol. 74, 2083–2094.
Corbi, F., Rivalta, E., Pinel, V., Maccaferri, F., Bagnardi, M., Acocella, V., 2015. How caldera collapse shapes the shallow emplacement and transfer of magma in active volcanoes. Earth Planet. Sci. Lett. 431, 287–293.
Corbi, F., Rivalta, E., Pinel, V., Maccaferri, F., Acocella, V., 2016. Understanding the link between circumferential dikes and eruptive fissures around calderas based on numerical and analog models. Geophys. Res. Lett. 43 (12), 6212–6219.
Cowie, P.A., Scholz, C.H., 1992. Growth of faults by accumulation of seismic slip. J. Geophys. Res. 97, 11085.
Currenti, G., Napoli, R., Di Stefano, A., Greco, F., Del Negro, C., 2011. 3D integrated geophysical modeling for the 2008 magma intrusion at Etna: Constraints on rheology and dike overpressure. Phys. Earth Planet. Inter. 185 (1–2), 44–52.
Dahm, T., 2000. Numerical simulations of the propagation path and the arrest of fluid-filled fractures in the Earth. Geophys. J. Int. 141 (3), 623–638.
Dawers, N.H., Anders, M.H., 1995. Displacement–length scaling and fault linkage. J. Struct. Geol. 17, 607–614.
De Beni, E., Branca, S., Coltelli, M., Groppelli, G., Wijbrans, J.R., 2011. 40Ar/39Ar isotopic dating of Etna volcanic succession. Ital. J. Geosci. 130 (3), 292–305.
Delaney, P., Pollard, D., Ziony, J., McKee, E., 1986. Field relations between dikes and joints: emplacement processes and paleostress analysis. J. Geophys. Res. 91, 4920–4938.
Døssing, A., Kolster, M.E., da Silva, E.L., Muxworthy, A.R., Petersen, J.T., Riishuus, M.S., 2024. Pre-existing structural control on the recent Holuhraun eruptions along the Bárðarbunga spreading center, Iceland. Scientific Rep. 14 (1), 3399.
Drymoni, K., Browning, J., Gudmundsson, A., 2021. Volcanotectonic interactions between inclined sheets, dykes, and faults at the Santorini Volcano, Greece. J. Volcanol. Geotherm. Res. 416, 107294.
Dumont, S., Klinger, Y., Socquet, A., Doubre, C., Jacques, E., 2017. Magma influence on propagation of normal faults: Evidence from cumulative slip profiles along Dabbahu-Manda-Hararo rift segment (Afar, Ethiopia). J. Struct. Geol. 95, 48–59.
Falsaperla, S., Neri, M., 2015. Seismic footprints of shallow dyke propagation at Etna, Italy. Sci. Rep. 5, 11908. https://doi.org/10.1038/srep11908.
Falsaperla, S., Alparone, S., D'Amico, S., Grazia, G., Ferrari, F., Langer, H., Sgroi, T., Spampinato, S., 2005. Volcanic tremor at Mt. Etna, Italy, preceding and accompanying the eruption of July–August, 2001. Pure Appl. Geophys. 162, 2111–2132.
Ferrari, L., Garduño, V.H., Neri, M., 1991. I dicchi della Valle del Bove, Etna: un metodo per stimare le dilatazioni di un apparato vulcanico. Mem. Soc. Geol. It 47, 495–508, 9 figg., 2 tabb.
Fialko, Y.A., Rubin, A.M., 1999. Thermal and mechanical aspects of magma emplacement in giant dike swarms. J. Geophys. Res. Solid Earth 104 (B10), 23033–23049.
Fiske, R.S., Jackson, E.D., 1972. Orientation and growth of Hawaiian volcanic rifts: the effect of regional structure and gravitational stresses. Proc. R. Soc. Lond. A Math. Phys. Sci. 329 (1578), 299–326.
Fittipaldi, M., Urbani, S., Neri, M., Trippanera, D., Acocella, V., 2019. Understanding the origin of magmatic necks: insights from Etna and analogue models. Bull. Volcanol. 81, 11. https://doi.org/10.1007/s00445-019-1273-1.
Galland, O., Holohan, E., de Vries, B.V.W., Burchardt, S., 2015. Laboratory modelling of volcano plumbing systems: a review. Phys. Geol. Shallow Magmatic Syst. 147–214.
Geshi, N., Neri, M., 2014. Dynamic feeder dyke systems in basaltic volcanoes: the exceptional example of the 1809 Etna eruption (Italy). Front. Earth Sci. 2, 13.
Glicken, H., Janda, R.J., Voight, B., 1980. Catastrophic landslide/debris avalanche of May 18, 1980, Mount St. Helens Volcano,[abs.]. EOS. Trans. Am. Geophys. Union 61 (46), 1135.
Goodman, R.E., 1991. Introduction to rock mechanics. John Wiley & Sons, 562 pp.
Greiner, S.H., Burchardt, S., Sigmundsson, F., Óskarsson, B.V., Galland, O., Geirsson, H., Rhodes, E., 2023. Interaction between propagating basaltic dikes and pre-existing fractures: A case study in hyaloclastite from Dyrfjöll, Iceland. J. Volcanol. Geotherm. Res. 442, 107891.
Groppelli, G., Tibaldi, A., 1999. Control of rock rheology on deformation style and slip-rate along the active Pernicana Fault, Mt. Etna, Italy. Tectonophysics 305 (4), 521–537.
Gudmundsson, A., 1983. Form and dimensions of dykes in eastern Iceland. Tectonophysics 95, 295–307.
Gudmundsson, A., 1986. Mechanical aspects of postglacial volcanism and tectonics of the Reykjanes Peninsula, southwest Iceland. J. Geophys. Res. Solid Earth 91 (B12), 12711–12721.
Gudmundsson, A., 2003. Surface stresses associated with arrested dykes in rift zones. Bull. Volcanol. 65, 606–619.
Gudmundsson, A., 2006. How local stresses control magma-chamber ruptures, dyke injections, and eruptions in composite volcanoes. Earth Sci. Rev. 79 (1–2), 1–31.
Gudmundsson, A., 2011a. Rock fractures in geological processes. Cambridge University Press.
Gudmundsson, A., 2011b. Deflection of dykes into sills at discontinuities and magma-chamber formation. Tectonophysics 500 (1–4), 50–64.
Gudmundsson, A., 2020. Volcano Tectonics: Understanding the structure, deformation and dynamics of volcanoes. Cambridge University Press.
Gudmundsson, A., 2022. The propagation paths of fluid-driven fractures in layered and faulted rocks. Geol. Mag. 159 (11−12), 1978–2001.
Gudmundsson, A., Friese, N., Galindo, I., Philipp, S.L., 2008. Dike-induced reverse faulting in a graben. Geology 36 (2), 123–126.
Guest, J.E., 1973. The summit of Mt Etna prior to the 1971 eruptions. Philos. Trans. R. Soc. Lond. 274A, 63–78.
Guest, J.E., Huntingdon, A.T., Wadge, G., Brander, J.L., Booth, B., Carter, S., Duncan, A., 1974. Recent eruption of Mount Etna. Nature 250, 385–387.
Guest, J.E., Chester, D.K., Duncan, A.M., 1984a. The Valle del Bove, Mount Etna: its origin and relation to the stratigraphy and structure of the volcano. J. Volcanol. Geotherm. Res. 21 (1–2), 1–23.
Guest, J.E., Wood, C., Greeley, R., 1984b. Lava tubes, terraces and megatumuli on the 1614–24 pahoehoe lava flow field, Mount Etna, Sicily. Bull. Volcanol. 47, 635–648.
Guldstrand, F., Burchardt, S., Hallot, E., Galland, O., 2017. Dynamics of surface deformation induced by dikes and cone sheets in a cohesive Coulomb brittle crust. J. Geophys. Res. Solid Earth 122 (10), 8511–8524.
Handin, J., 1966. Strength and ductility. Handb. Phys. Constants 97, 223–289.
Harknett, J., Whitworth, M., Rust, D., Krokos, M., Kearl, M., Tibaldi, A., et al., 2022. The use of immersive virtual reality for teaching fieldwork skills in complex structural terrains. J. Struct. Geol. 163, 104681.
Hjartardóttir, Á.R., Einarsson, P., Gudmundsson, M.T., Högnadóttir, T., 2016. Fracture movements and graben subsidence during the 2014 Bárðarbunga dike intrusion in Iceland. J. Volcanol. Geotherm. Res. 310, 242–252.
Hjartardóttir, Á.R., Dürig, T., Parks, M., Drouin, V., Eyjólfsson, V., Reynolds, H., Einarsson, P., Hlíðar Jensen, E., Vilhelm Óskarsson, B., Belart, J.M.C., Ruch, J., Gies, N.B., Pedersen, G.B., 2023. Pre-existing fractures and eruptive vent openings during the 2021 Fagradalsfjall eruption, Iceland. Bull. Volcanol. 85 (10), 56.
Holohan, E.P., Troll, V.R., Walter, T.R., Münn, S., McDonnell, S., Shipton, Z.K., 2005. Elliptical calderas in active tectonic settings: an experimental approach. J. Volcanol. Geotherm. Res. 144 (1–4), 119–136.
Horsfield, W.T., 1977. An experimental approach to basement-controlled faulting. Geol. Mijnb. 56 (4), 363–370.

Hoshino, K., Koide, H., Inami, K., Iwamura, S., Mitsui, S., 1972. Me-chanical properties of Japanese Tertiary sedimentary rocks under high confining pressures, Rep. In: 244, 200 pp. Geol. Surv. of Japan, Kawasaki.
Houghton, B.F., Schmincke, H.-U., 1989. Rothenberg scoria cone, East Eifel: a complex Strombolian and phreatomagmatic volcano. Bull. Volcanol. 52, 28–48.
Ito, G., Martel, S.J., 2002. Focusing of magma in the upper mantle through dike interaction. Journal of Geophysical Research: Solid. Earth 107 (B10), ECV–6.
Jaeger, J.C., Cook, N.G., 1969. Fundamentals of rock mechanics. Methuen & Co. Ltd., London, p. 513.
Kattenhorn, S.A., Pollard, D.D., 2001. Integrating 3-D seismic data, field analyses, and mechanical models in the analyses of segmented normal faults in the Wytch Farm oil field, southern England, United Kingdom. AAPG Bull. 85, 1183–1210.
Kavanagh, J.L., Menand, T., Sparks, R.S.J., 2006. An experimental investigation of sill formation and propagation in layered elastic media. Earth Planet. Sci. Lett. 245 (3–4), 799–813.
Kervyn, M., Ernst, G.G.J., van Wyk de Vries, B., Mathieu, L., Jacobs, P., 2009. Volcano load control on dyke propagation and vent distribution: Insights from analogue modeling. Journal of Geophysical Research: Solid. Earth 114 (B3).
King Hubbert, M., 1951. Mechanical basis for certain familiar geologic structures. Geol. Soc. Am. Bull. 62 (4), 355–372.
Knipe, R.J., 1992. Faulting processes and fault seal. In: Structural and Tectonic Modelling and its Application to Petroleum Geology. Elsevier, pp. 325–342.
Krantz, R.W., 1991. Measurements of friction coefficients and cohesion for faulting and fault reactivation in laboratory models using sand and sand mixtures. Tectonophysics 188 (1–2), 203–207.
La Sicilia, 1947. In: Sanfilippo, Domenico (Ed.), Issues of 26 and 27 February, 6 and 9 March, p. 1. Catania, Italy.
Lanzafame, G., Neri, M., Acocella, V., Billi, A., Funiciello, R., Giordano, G., 2003. Structural features of the July–August 2001 Mount Etna eruption: evidence for a complex magma supply system. J. Geol. Soc. 160 (4), 531–544.
Le Corvec, N., Menand, T., Lindsay, J., 2013. Interaction of ascending magma with pre-existing crustal fractures in monogenetic basaltic volcanism: an experimental approach. J. Geophys. Res. Solid Earth 118, 968–984.
Lister, J.R., Kerr, R.C., 1991. Fluid-mechanical models of crack propagation and their application to magma transport in dykes. J. Geophys. Res. Solid Earth 96 (B6), 10049–10077.
Lo Giudice, E., Patane, G., Rasa, R., Romano, R., 1982. The structural framework of Mount Etna. Mem. Soc. Geol. Ital. 23, 125–158.
Luongo, G., Cubellis, E., Obrizzo, F., Petrazzuoli, S.M., 1991. A physical model for the origin of volcanism of the Tyrrhenian margin: the case of the Neapolitan area. Volcanol. Geotherm. Res. 48, 173–185.
Maccaferri, F., Bonafede, M., Rivalta, E., 2011. A quantitative study of the mechanisms governing dike propagation, dike arrest and sill formation. J. Volcanol. Geotherm. Res. 208 (1–2), 39–50.
Maccaferri, F., Rivalta, E., Passarelli, L., Aoki, Y., 2016. On the mechanisms governing dike arrest: Insight from the 2000 Miyakejima dike injection. Earth Planet. Sci. Lett. 434, 64–74.
Maerten, L., Willemse, E.J.M., Pollard, D.D., Rawnsley, K., 1999. Slip distributions on intersecting normal faults. J. Struct. Geol. 21, 259–271.
Magee, C., Jackson, C.A.L., 2021. Can we relate the surface expression of dike-induced normal faults to subsurface dike geometry? Geology 49 (4), 366–371.
Magee, C., Stevenson, C.T., O'Driscoll, B., Petronis, M.S., 2012. Local and regional controls on the lateral emplacement of the Ben Hiant Dolerite intrusion, Ardnamurchan (NW Scotland). J. Struct. Geol. 39, 66–82.
Malaguti, A.B., Branca, S., Speranza, F., Coltelli, M., Del Carlo, P., Renzulli, A., 2023. Age of the Valle del Bove formation and chronology of the post-collapse flank eruptions, Etna volcano (Italy). J. Volcanol. Geotherm. Res. 434, 107752.
Manighetti, I., King, G.C.P., Gaudemer, Y., Scholz, C.H., Doubre, C., 2001. Slip accumulation and lateral propagation of active normal faults in Afar. J. Geophys. Res. Solid Earth 106 (B7), 13667–13696.
Manighetti, I., King, G., Sammis, C.G., 2004. The role of off-fault damage in the evolution of normal faults. Earth Planet. Sci. Lett. 217 (3–4), 399–408.
Mannini, S., Ruch, J., Hazlett, R.W., Downs, D.T., Parcheta, C.E., Lundblad, S.P., Anderson, J.L., Perroy, L., Oestreicher, N., 2024. Tracking magma pathways and surface faulting in the Southwest Rift Zone and the Koa'e fault system (Kīlauea volcano, Hawai'i) using photogrammetry and structural observations. Bull. Volcanol. 86 (5), 45.
Mansfield, C., Cartwright, J., 2001. Fault growth by linkage: observations and implications from analogue models. J. Struct. Geol. 23, 745–763.
Marchal, D., Guiraud, M., Rives, T., 2003. Geometric and morphologic evolution of normal fault planes and traces from 2D to 4D data. J. Struct. Geol. 25, 135–158.
Mastin, L.G., Pollard, D.D., 1988. Surface deformation and shallow dike intrusion processes at Inyo Craters, Long Valley, California. J. Geophys. Res. Solid Earth 93 (B11), 13221–13235.
Mathieu, L., van Wyk de Vries, B., Holohan, E.P., Troll, V.R., 2008. Dykes, cups saucers and sills: Analogue experiments on magma intrusion into brittle rocks. Earth Planet. Sci. Lett. 271, 1–13.
Menand, T., Tait, S.R., 2002. The propagation of a buoyant liquid-filled fissure from a source under constant pressure: An experimental approach. Journal of Geophysical Research: Solid. Earth 107 (B11), ECV–16.
Merle, O., 2015. The scaling of experiments on volcanic systems. Front. Earth Sci. 3, 26.
Montanari, D., Bonini, M., Corti, G., Agostini, A., Del Ventisette, C., 2017. Forced folding above shallow magma intrusions: Insights on supercritical fluid flow from analogue modelling. J. Volcanol. Geotherm. Res. 345, 67–80.
Montgomery-Brown, E.K., Miklius, A., 2021. Periodic dike intrusions at Kīlauea volcano, Hawai'i. Geology 49, 397–401. https://doi.org/10.1130/G47970.1.
Muller, J.R., Ito, G., Martel, S.J., 2001. Effects of volcano loading on dike propagation in an elastic half-space. J. Geophys. Res. Solid Earth 106 (B6), 11101–11113.
Murray, J.B., 1980a. The Bocca Nuova: its history and possible causes of the 12 September 1979 explosion. UK Res Mount Etna, 1977–1979. Philos. Trans. R. Soc. Lond. 274A, 46–49.
Murray, J.B., 1980b. Changes in the North-east Crater region 1976–78. UK Res Mount Etna, 1977–1979. Philos. Trans. R. Soc. Lond. 274A, 37–43.
Neri, M., Lanzafame, G., Acocella, V., 2008. Dyke emplacement and related hazard in volcanoes with sector collapse: the 2007 Stromboli (Italy) eruption. J. Geol. Soc. 165 (5), 883–886.
Nicol, A., Watterson, J., Walsh, J.J., Childs, C., 1996. The shapes, major axis orientations and displacement patterns of fault surfaces. J. Struct. Geol. 18 (2), 235–248.
Paquet, F., Dauteuil, O., Hallot, E., Moreau, F., 2007. Tectonics and magma dynamics coupling in a dyke swarm of Iceland. J. Struct. Geol. 29 (9), 1477–1493.
Pedicini, M., Bonali, F.L., Corti, N., Tibaldi, A., 2024. Rift structure and development: The Krafla Fissure Swarm (Northern Iceland). J. Struct. Geol. 105332.
Peltier, A., Ferrazzini, V., Staudacher, T., Bachelery, P., 2005. Imaging the dynamics of dyke propagation prior to the 2000–2003 flank eruptions at Piton de La Fournaise, Reunion Island. Geophys. Res. Lett. 32, L22302. https://doi.org/10.1029/2005GL023720.
Pinel, V., Jaupart, C., 2004. Magma storage and horizontal dyke injection beneath a volcanic edifice. Earth Planet. Sci. Lett. 221 (1–4), 245–262.
Pinel, V., Carrara, A., Maccaferri, F., Rivalta, E., Corbi, F., 2017. A two-step model for dynamical dike propagation in two dimensions: Application to the July 2001 Etna eruption. J. Geophys. Res. Solid Earth 122 (2), 1107–1125.
Pollard, D.D., Segall, P., 1987. Theoretical displacements and stresses near fractures in rock: with applications to faults, joints, veins, dikes, and solution surfaces. Fract. Mech. Rock 277 (349), 277–349.
Pollard, D.D., Delaney, P.T., Duffield, W.A., Endo, E.T., Okamura, A.T., 1983. Surface deformation in volcanic rift zones. In: Developments in Geotectonics, 19. Elsevier, pp. 541–584.
Ponte, G., 1947a. L'eruzione etnea del Febbraio 1947 e le vicende dell'Istituto Vulcanologico dell'Università di Catania. L'Universo 27, 1–9.
Ponte, G., 1947b. Sulla recente eruzione dell'Etna. Lettere alla direzione. Catania 12 aprile 1947.
Ponte, G., 1948. L'eruzione dell'Etna del febbraio-marzo 1947. Ann. di Geofis., Vol. I, N. I, 1948.
Proietti, C., De Beni, E., Cantarero, M., Civico, R., Palano, M., Paratore, M., Massaro, G., 2023, December. 150 years of Etna Summit Craters through a photogrammetry-based time machine. In: AGU Fall Meeting Abstracts, vol. 2023. No. 151, pp. V13D-0151.
Ramberg, H., 1971. Dynamic models simulating rift valleys and continental drift. Lithos 4 (3), 259–276.
Rivalta, E., Böttinger, M., Dahm, T., 2005. Buoyancy-driven fracture ascent: Experiments in layered gelatine. J. Volcanol. Geotherm. Res. 144 (1–4), 273–285.
Roche, V., Homberg, C., Rocher, M., 2012. Fault displacement profiles in multilayer systems: from fault restriction to fault propagation. Terra Nova 24 (6), 499–504.
Romano, R., Sturiale, C., 1982. The historical eruptions of Mt. Etna (volcanological data). Mem. Soc. Geol. Ital. 23, 75–97.
Rossetti, F., Storti, F., Salvini, F., 2000. Cenozoic non coaxial transtension along the western shoulder of the Ross Sea, Antarctica, and the emplacement of Mc Murdo dyke arrays. Terra Nova 12, 60–66.
Rubin, A.M., 1993. Tensile fracture of rock at high confining pressure: implications for dike propagation. J. Geophys. Res. Solid Earth 98 (B9), 15919–15935.
Rubin, A.M., Pollard, D.D., 1987. Origins of blade-like dikes in volcanic rift zones. US Geol. Surv. Prof. Pap. 1350 (2), 1449–1470.
Rubin, A.M., Pollard, D.D., 1988. Dike-induced faulting in rift zones of Iceland and Afar. Geology 16 (5), 413–417.
Ruch, J., Wang, T., Xu, W., Hensch, M., Jónsson, S., 2016. Oblique rift opening revealed by reoccurring magma injection in central Iceland. Nat. Commun. 7, 12352.
Rust, D., Neri, M., 1996. The boundaries of large-scale collapse on the flanks of Mount Etna, Sicily. Geol. Soc. Lond., Spec. Publ. 110 (1), 193–208.
Sato, M., Hamaguchi, H., 2006. Weak long-lived ground deformation related to Iwate volcanism revealed by Bayesian decomposition of strain, tilt and positioning data. J. Volcanol. Geotherm. Res. 155 (3–4), 244–262.
Schlagenhauf, A., Manighetti, I., Malavieille, J., Dominguez, S., 2008. Incremental growth of normal faults: insights from a laser-equipped analog experiment. Earth Planet. Sci. Lett. 273, 299–311. https://doi.org/10.1016/j.epsl.2008.06.042.
Scholz, C.H., 2002. The Mechanics of Earthquakes and Faulting. Cambridge University Press.
Schultz, R.A., 1996. Relative scale and the strength and deformability of rock masses. J. Struct. Geol. 18 (9), 1139–1149.
Sigmundsson, F., Hooper, A., Hreinsdóttir, S., Vogfjörd, K.S., Ófeigsson, B.G., Heimisson, E.R., Dumont, S., Parks, M., Spaans, K., Gudmundsson, G.B., Drouin, V., Árnadóttir, T., Jónsdóttir, K., Gudmundsson, M.T., Högnadóttir, T., Fridriksdóttir, H. M., Hensch, M., Einarsson, P., Magnússon, E., Samsonov, S., Brandsdóttir, B., White, R.S., Ágústsdóttir, T., Greenfield, T., Green, R.G., Hjartardóttir, Á.R., Pedersen, R., Bennett, R.A., Geirsson, H., La Femina, P.C., Björnsson, H., Pálsson, F., Sturkell, E., Bean, C.J., Möllhoff, M., Braiden, A.K., Eibl, E.P.S., 2015. Segmented lateral dyke growth in a rifting event at Bárðarbunga volcanic system, Iceland. Nature 517 (7533), 191–195.
Silvestri, O., 1874. Notizie sulla eruzione dell'Etna del 29 Marzo 1874. Boll. R. Comit. It. 5, 312–322.
Silvestri, S.C., 1949. L'eruzione dell'Etna del 1947. Bull. Volcanol. 9 (1), 81–111.
Spacapan, J.B., Galland, O., Leanza, H.A., Planke, S., 2016. Control of strike-slip fault on dyke emplacement and morphology. J. Geol. Soc. 173, 573–576.

Staudacher, T., Ferrazzini, V., Peltier, A., Kowalski, P., Boissier, P., Catherine, P., Lauret, F., Massin, F., 2009. The April 2007 eruption and the Dolomieu crater collapse, two major events at Piton de la Fournaise (La Réunion Island, Indian Ocean). J. Volcanol. Geotherm. Res. 184, 126–137. https://doi.org/10.1016/j.jvolgeores.2008.11.005.

Swanson, D. A., Fiske, R. S., Thornber, C. R., & Poland, M. P. (2019). Dikes in the Koa'e fault system, and the Koa'e–east rift zone structural grain at Kīlauea Volcano, Hawai'i. Field Volcanology: A Tribute to the Distinguished Career of Don Swanson (Edts: M. P. Poland, M. O. Garcia, V. E. Camp, A. Grunder), GSA Special Papers 538.

Takada, A., 1990. Experimental study on propagation of liquid-filled crack in gelatin: Shape and velocity in hydrostatic stress condition. J. Geophys. Res. Solid Earth 95 (B6), 8471–8481.

Tentler, T., Mazzoli, S., 2005. Architecture of normal faults in the rift zone of central north Iceland. J. Struct. Geol. 27 (9), 1721–1739.

Thiele, S.T., Cruden, A.R., Zhang, X., Micklethwaite, S., Matchan, E.L., 2021. Reactivation of magma pathways: Insights from field observations, geochronology, geomechanical tests, and numerical models. J. Geophys. Res. Solid Earth 126 (5) e2020JB021477.

Tibaldi, A., 2015. Structure of volcano plumbing systems: a review of multi-parametric effects. J. Volcanol. Geotherm. Res. 298, 85–135.

Tibaldi, A., Groppelli, G., 2002. Volcano-tectonic activity along structures of the unstable NE flank of Mt. Etna (Italy) and their possible origin. J. Volcanol. Geotherm. Res. 115 (3–4), 277–302.

Tibaldi, A., Pasquare Mariotto, F., Papanikolaou, D., Nomikou, P., 2008a. Tectonics of Nisyros Island, Greece, by field and offshore data, and analogue modelling. J. Struct. Geol. 30 (12), 1489–1506.

Tibaldi, A., Vezzoli, L., Pasquaré Mariotto, F., Rust, D., 2008b. Strike-slip fault tectonics and the emplacement of sheet–laccolith systems: the Thverfell case study (SW Iceland). J. Struct. Geol. 30 (3), 274–290.

Tibaldi, A., Pasquaré, Mariotto F., Rust, D., 2011. New insights into the cone sheet structure of the Cuillin Complex, Isle of Skye, Scotland. J. Geol. Soc. 168, 689–704.

Tibaldi, A., Bonali, F.L., Einarsson, P., Hjartardóttir, Á.R., Pasquaré Mariotto, F., 2016. Partitioning of Holocene kinematics and interaction between the Theistareykir Fissure Swarm and the Husavik-Flatey Fault, North Iceland. J. Struct. Geol. 83, 134–155.

Tibaldi, A., Bonali, F.L., Pasquaré Mariotto, F., Russo, E., Tenti, L.R., 2019. The development of divergent margins: Insights from the North Volcanic Zone, Iceland. Earth Planet. Sci. Lett. 509, 1–8.

Tibaldi, A., Bonali, F.L., Vitello, F., Delage, E., Nomikou, P., Antoniou, V., Becciani, U., Wyk, Van, de Vries, B., Krokos, M., Whitworth, M., 2020a. Real world–based immersive Virtual Reality for research, teaching and communication in volcanology. Bull. Volcanol. 82, 1–12.

Tibaldi, A., Corti, N., Bonali, F.L., Pasquaré Mariotto, F., Russo, E., 2020b. Along-rift propagation of Pleistocene-Holocene faults from a central volcano. J. Struct. Geol. 141, 104201.

Tibaldi, A., Bonali, F.L., Russo, E., Fallati, L., 2020c. Surface deformation and strike-slip faulting controlled by dyking and host rock lithology: a compendium from the Krafla Rift, Iceland. J. Volcanol. Geotherm. Res. 106835.

Tibaldi, A., Corti, N., De Beni, E., Bonali, F.L., Falsaperla, S., Langer, H., Neri, M., Cantarero, M., Reitano, D., Fallati, L., 2021. Mapping and evaluating kinematics and stress/strain field at active faults and fissures: a comparison between field and drone data at NE Rift, Mt Etna (Italy). Solid Earth 12 (4), 801–816.

Tibaldi, A., Bonali, F.L., Corti, N., Russo, E., Drymoni, K., De Beni, E., Branca, S., Neri, M., Cantarero, M., Mariotto, F.P., 2022. Surface deformation during the 1928 fissure eruption of Mt. Etna (Italy): Insights from field data and FEM numerical modelling. Tectonophysics 837, 229468.

Tortini, R., Bonali, F.L., Corazzato, C., Carn, S.A., Tibaldi, A., 2014. An innovative application of the Kinect in Earth sciences: quantifying deformation in analogue modelling of volcanoes. Terra Nova 26 (4), 273–281.

Townsend, M.R., Pollard, D.D., Smith, R.P., 2017. Mechanical models for dikes: A third school of thought. Tectonophysics 703, 98–118.

Trippanera, D., Acocella, V., Ruch, J., 2014. Dike-induced contraction along oceanic and continental divergent plate boundaries. Geophys. Res. Lett. 41 (20), 7098–7104.

Trippanera, D., Ruch, J., Acocella, V., Rivalta, E., 2015. Experiments of dike-induced deformation: Insights on the long-term evolution of divergent plate boundaries. J. Geophys. Res. Solid Earth 120 (10), 6913–6942.

Urlaub, M., Petersen, F., Gross, F., Bonforte, A., Puglisi, G., Guglielmino, F., Krastel, S., Lange, D., Kopp, H., 2018. Gravitational collapse of Mount Etna's southeastern flank. Science. Advances 4 (10), eaat9700.

Valentine, G.A., Krogh, K.E., 2006. Emplacement of shallow dikes and sills beneath a small basaltic volcanic center–The role of pre-existing structure (Paiute Ridge, southern Nevada, USA). Earth Planet. Sci. Lett. 246 (3–4), 217–230.

Walsh, J.J., Bailey, W.R., Childs, C., Nicol, A., Bonson, C.G., 2003. Formation of segmented normal faults: a 3-D perspective. J. Struct. Geol. 25, 1251–1262.

Walter, T.R., Troll, V.R., 2001. Formation of caldera periphery faults: an experimental study. Bull. Volcanol. 63, 191–203.

Waltershausen, W.S., 1880. Der Aetna, vol. 1 and 2. Engelman, Leipzig.

Watanabe, T., Masuyama, T., Nagaoka, K., Tahara, T., 2002. Analog experiments on magma-filled cracks Competition between external stresses and internal pressure. Earth Planets Space 54 (12), 1247–1261.

Willemse, E.J., 1997. Segmented normal faults: correspondence between three dimensional mechanical models and field data. J. Geophys. Res. 102, 675–692.

Wright, T.J., Ebinger, C., Biggs, J., Ayele, A., Yirgu, G., Keir, D., Stork, A., 2006. Magma-maintained rift segmentation at continental rupture in the 2005 Afar dyking episode. Nature 442 (7100), 291–294.

Ziv, A., Rubin, A.M., Agnon, A., 2000. Stability of dike intrusion along preexisting fractures. J. Geophys. Res. Solid Earth 105 (B3), 5947–5961.

Zwaan, F., Schreurs, G., 2022. Analogue modeling of continental rifting: an overview. In: Continental Rifted Margins, 1. John Wiley, pp. 309–343.